

AD A121764

(12)

RADC-
Interim Report
September 1982

**STUDY OF THE PHYSICS OF INSULATING FILMS AS RELATED TO THE
RELIABILITY OF METAL-OXIDE-SEMICONDUCTOR (MOS) DEVICES**

SEMI-ANNUAL TECHNICAL REPORT
December 1, 1981 - May 31, 1982

S. R. Brorson
I. F. Chang
J. F. DeGelormo
D. J. DiMaria
D. W. Dong
D. B. Dove
C. Falcony
A. Hartstein
E. A. Irene
S. K. Lai
D. J. Robbins
Z. Weinberg

**IBM T.J. WATSON RESEARCH CENTER
YORKTOWN HEIGHTS, NY 10598**

**SPONSORED BY
DEFENSE ADVANCED RESEARCH PROJECTS AGENCY (DoD)
ARPA Order No. 4012**

**UNDER CONTRACT No. MDA903-81-C-0100 ISSUED BY
DEPARTMENT OF ARMY, DEFENSE SUPPLY SERVICE-WASHINGTON,
WASHINGTON, DC 20310**

Approved for public release; distribution unlimited.

DTIC
ELECTED
NOV 24 1982
S E D
E

The views and conclusions contained in this document are those of the authors and should not be interpreted as representing the official policies, either expressed or implied, of the Defense Advanced Research Agency or the United States Government.

DTIC FILE COPY
82 11 24 018

UNCLASSIFIED

SECURITY CLASSIFICATION OF THIS PAGE (When Data Entered)

REPORT DOCUMENTATION PAGE		READ INSTRUCTIONS BEFORE COMPLETING FORM
1. REPORT NUMBER RADC-	2. GOVT ACCESSION NO. A5 A121 764	3. RECIPIENT'S CATALOG NUMBER
4. TITLE (and Subtitle) STUDY OF THE PHYSICS OF INSULATING FILMS AS RELATED TO THE RELIABILITY OF METAL-OXIDE-SEMICONDUCTOR (MOS) DEVICES		5. TYPE OF REPORT & PERIOD COVERED SEMI-ANNUAL TECHNICAL REPORT 12/1/81 - 5/31/82
		6. PERFORMING ORG. REPORT NUMBER
7. AUTHOR(s) S.R. Brorson, I.F. Chang, J.F. DeGelormo, D.J. DiMaria, D.W. Dong, D.B. Dove, C. Falcony, A. Hartstein, E.A. Irene, S.K. Lai, D.J. Robbins, and Z. Weisberg		8. CONTRACT OR GRANT NUMBER(s) MDA903-81-C-0100
9. PERFORMING ORGANIZATION NAME AND ADDRESS IBM Thomas J. Watson Research Center P.O. Box 218 Yorktown Heights, NY 10598		10. PROGRAM ELEMENT, PROJECT, TASK AREA & WORK UNIT NUMBERS
11. CONTROLLING OFFICE NAME AND ADDRESS Advanced Research Projects Agency 1400 Wilson Blvd. Arlington, VA 22209		12. REPORT DATE September 1982
		13. NUMBER OF PAGES 76
14. MONITORING AGENCY NAME & ADDRESS (if different from Controlling Office) Deputy for Electronic Technology (RADC/ESR) Hanscom AFB, MA 01730 Monitor: Dr. John C. Garth/ESR		15. SECURITY CLASS. (of this report) UNCLASSIFIED
		15a. DECLASSIFICATION DOWNGRADING SCHEDULE N/A
16. DISTRIBUTION STATEMENT (of this Report) Approved for public release; distribution unlimited		
17. DISTRIBUTION STATEMENT (of the abstract entered in Block 20, if different from Report) SAME		
18. SUPPLEMENTARY NOTES RADC Project Engineer: J.C. Garth (ESR)		
19. KEY WORDS (Continue on reverse side if necessary and identify by block number) Interface states, Electrically-alterable read-only-memories, electroluminescent devices, image force theory, oxidation.		
20. ABSTRACT (Continue on reverse side if necessary and identify by block number) This report contains a discussion of the effect of the gate metal on the build up of interface states at the Si-SiO ₂ interface. A method for reducing electron trapping in SiO ₂ is described that significantly increases the cyclability of electrically-alterable read-only storage devices. A new low voltage electroluminescent device has been built that uses Si rich SiO ₂ charge injectors. Photon-assisted-tunneling and internal photoemission measurements have been made on metal-oxide-semiconductor samples. A quantum mechanical image force theory has been used to explain the results. Studies of the temperature dependence of the oxidation rate of silicon indicate that there are two oxidant species responsible.		

UNCLASSIFIED

SECURITY CLASSIFICATION OF THIS PAGE(When Data Entered)

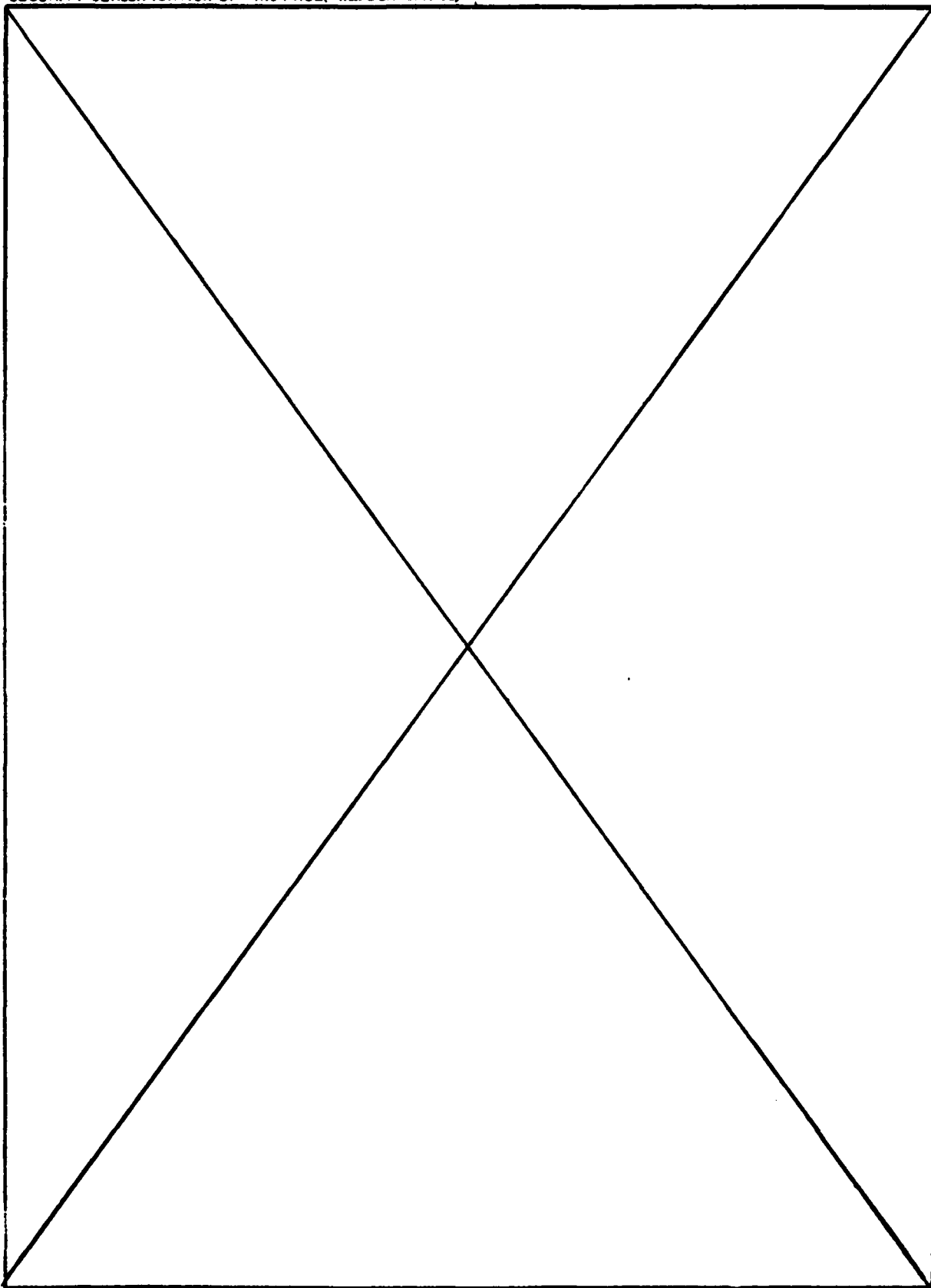


TABLE OF CONTENTS

1. Introduction	Page 4
2. Effects of Gate Metal on Interface Effects in MOS Systems After Electron Trapping	Page 8
3. Extended Cyclability in Electrically-Alterable-Read-Only-Memories	Page 20
4. A New Low-Voltage Si-Compatible Electroluminescent Device	Page 30
5. Experimental Test of the Quantum Mechanical Image Force Theory	Page 43
6. Evidence for a Parallel Path Oxidation Mechanism at the Si-SiO ₂ Interface	Page 70
7. Silicon Oxidation Studies: Measurement of the Diffusion of Oxidant in SiO ₂ Films	Page 72

Accession For	
NTIS GRA&I	<input checked="" type="checkbox"/>
DTIC TAB	<input type="checkbox"/>
Unannounced	<input type="checkbox"/>
Justification	
By _____	
Distribution/	
Availability Codes	
Dist	Avail and/or Special
A	



INTRODUCTION

Considerable work has been done on studies relating to the build-up of positive charge at the Si-SiO₂ interface resulting from the application of high electric fields, the passage of electron current through MOS devices, and the exposure to radiation. Previous work has shown that this can result from the application of non-penetrating UV (with energy > 9 eV) to the outside of the oxide and that water related species in the SiO₂ can significantly accelerate the process. One of the mechanisms proposed is that atomic hydrogen, released during the process of electron trapping on water related sites in the SiO₂, migrates to the Si-SiO₂ interface and results in the generation of the positive charge. S. Lai has studied the use of other metals in comparison with Al for the gate electrode. The original proposal was to use Ti which is known to be a getter for hydrogen and he found a reduction in the positive charge generation; however, this also occurred with the use of Au as the electrode. The net conclusion is that Al plays a unique and vital role in increasing the positive charge effect. This work is described in the first paper included in this report.

It is well known that the number of useful read-write cycles in contemporary floating gate devices is limited by electron trapping in the SiO₂. Previous work under this contract has shown that the number of cycles increases as improved processing procedures are used; Nevertheless, these improved procedures seemed to indicate ultimate limitations in the number of useful read/write cycles to be in the range of 10⁶ cycles. Recent work on the contract has shown that this is not the limit and can be significantly extended with useful write/erase windows remaining up to 10¹⁰ cycles. The means for doing this consists of using Si-rich SiO₂ (with a smaller concentration of excess Si) in the intervening oxide as well as in the charge injector regions. This significant development opens up an entirely new range of applications for these devices. It can be expected that the use of the excess Si in these layers might result in a deterioration of the charge retention characteristic which certainly occurs if too much Si is used; however, our work has shown that a useful range of composition exists with excellent charge retention characteristics. Trapping studies have shown that the effect of the excess Si is to essentially eliminate the build-up of negative charge in the SiO₂ due to charge trapping. Experiments are underway to investigate the physical mechanism responsible for these observations. This work is described in the paper by DiMaria, Dong, Falcony and Brorson.

We have been gratified to observe that DEIS structures can be made using a Plasma-Therm CVD system as well as the usual CVD process. This supports our earlier conclusion

that the characteristics of these devices are not strongly process dependent and that comparable results can be obtained in different systems.

The Si rich charge injectors have enabled us to inject surprisingly large current densities into SiO_2 without introducing destructive electrical breakdown (current densities $> 1 \text{ amp/cm}^2$). The use of these injectors in conjunction with electroluminescent materials (ZnS:Mn) have resulted in a new type of electroluminescent device. These devices have produced a useful luminance of 79 fL at 48 volts which is a significantly lower voltage than for conventional AC thin film or DC devices. The potential energy step at the $\text{SiO}_2\text{-ZnS}$ interface (due to the larger energy gap of SiO_2 compared to ZnS) also offers the possibility of injecting hot electrons into the ZnS. This suggests a solid state analogue to the cathode ray tube. This work is described in the paper by Robbins, et al.

Photon-assisted tunneling and internal photoemission measurements have been made by Hartstein, Weinberg and DiMaria on the same samples. The effective barrier height as determined by the internal photoemission measurements is about .3 eV higher. A quantum mechanical image force theory has been developed to explain this result.

E. Irene has proposed a viscous flow model to explain his observation that SiO_2 grown at 800°C has a higher density than SiO_2 grown at 1000°C . Two papers by Irene are included in this report. The first one suggests that there are two oxidation species at the Si- SiO_2 interface that act in parallel. This is based on the nature of the curvature for the Arrhenius plots. The other paper suggests a method for measuring the diffusion of the oxidant in SiO_2 based on time lag measurements using in situ ellipsometry. Results of these studies are given in the paper.

We are excited about some new work involving the measurement of the spectra generated by electrons falling from the conduction band of SiO_2 into the metal gate electrode and creating surface plasmons. This is an inverse photo-emission process and offers new vistas for studies of the hot electron distribution in SiO_2 at high electric fields and on the nature of the metal-insulator interface. This work requires a means for obtaining a large electron current flow through the SiO_2 which can be accomplished using our Si rich charge injectors. The results of these studies by Theis, Kirtley and DiMaria will be presented in our next report.

Papers Published:

1. D.J. Robbins, C. Falcony, D.J. DiMaria, D.W. Dong, J.F. DeGelormo, I.F. Chang and D.B. Dove, "A New Low-Voltage Si-Compatible Electroluminescent Device", IEEE Electron Dev. Lett. EDL-3, 147 (1982).
2. A. Hartstein, Z.A. Weinberg and D.J. DiMaria, "Experimental Test of the Quantum Mechanical Image-Force Theory", Phys. Rev. B25, 7174 (1982).
3. D.J. DiMaria, D.W. Dong, C. Falcony and S.D. Brorson, "Extended Cyclability in Electrically-Alterable Read-Only-Memories", IEEE Electron Device Lett. EDL-13, 191 (1982).
4. C. Falcony, D.J. DiMaria and C.R. Guarnieri, "Enhanced Electron Injection into SiO_2 Layers Using Granular Metal Films", J. Appl. Phys. 53, 5347 (1982).

Presentations Made:

1. **D.J. DiMaria, C. Falcony, D.W. Dong and K.M. DeMeyer, "The Effects of Charge Trapping on DEIS EAROMs and Ways to Minimize It", 5th Non-Volatile Semiconductor Memory Workshop, March 7-10, 1982, Monterey, California.**
2. **C. Falcony, "Application of High Current Injectors Into SiO₂ in Memory Structures", Seminar at RCA David Sarnoff Research Center, Princeton, NJ, February 15, 1982.**
3. **D.J. DiMaria, "Mixed Phase Oxides in EAROM Applications", 10th Electronic Materials Symposium, Santa Clara, California, April 5, 1982.**
4. **D.J. DiMaria, "Insulator Physics and Engineering", Physics Department Seminar at the University of North Carolina, Chapel Hill, NC, May 18, 1982.**
5. **D.J. Robbins, C. Falcony, D.J. DiMaria, D.W. Dong, J.F. DeGelormo, I.F. Chang and D.B. Dove, "A New Low-Voltage Si-Compatible Electroluminescent Device" at Society for Information Display (SID), San Diego, CA, May 11-13, 1982.**

**Effects of Gate Metal on Interface Effects in
MOS Systems after Electron Trapping***

S.K. Lai

I.B.M. Thomas J. Watson Research Center
Yorktown Heights, New York 10598

Technical Assistance by J.A. Calise and Silicon Processing Facility

Abstract:

In the study of electron trapping in silicon dioxide, a turn-around effect in the flatband voltage shift as a function of injected electrons has been reported. Most of the reported work was on capacitors with aluminum gates. When polysilicon gates were used, very little electron trapping and turn-around effect was observed. The difference was explained by the decrease in the density of water related traps after the additional high temperature process in polysilicon deposition and doping. In the present experiment, gate metals other than aluminum were used. It was shown that even though the density of electron traps was not changed significantly, a large turn-around effect was only observed when aluminum gate was used. This result seems to imply that aluminum is mostly responsible for the slow state generation and turn-around effect.

* This work was sponsored by the Defense Advance Research Projects Agency (DoD) ARPA Order No. 4012 under Contract No. MDA903-81-C-0100 issued by Department of Army, Defense Supply Service-Washington, Washington, DC 20310.

In the study of the process dependence of electron trapping in silicon dioxide, a turn-around effect in the flatband voltage shift as a function of injected electrons has been observed¹⁻⁴. The turn-around effect was studied in detail and was shown to be due to the generation of fast and slow interface trap states at the silicon-silicon dioxide interface⁵. The fast states were donor states below midgap and acceptor states above midgap and were positively charged around flatband for P type silicon. The slow states were donor states and depending on the bias conditions, they were filled by electrons to different levels giving rise to a net positive charge at the silicon-silicon dioxide interface. Together with the fast states, the total positive charge at the interface compensated the negative charge from electrons trapped in the bulk of the oxide to give the turn-around effect.

Even though the charge components that give rise to the turn-around effect have been identified, the origin of the interface charge is still not known. From the evidence collected so far, the interface trap generation is related to electron trapping in the bulk of the oxide. In one experiment⁶, when the density of electron traps in the bulk of silicon dioxide was reduced by high temperature anneal in dry nitrogen, the generation of interface traps, both fast and slow states, were also reduced. In another experiment, Pang *et al.*⁷ used internal photoemission at low electric field to study the interface effects and they showed that there was a thickness dependence in the interface trap generation, showing a bulk dependence.

There were basically two models proposed so far to explain the turn-around effect. The first model was based on the observation made by Nicollian *et al.*⁸ that hydrogen was released after electron trapping in silicon dioxide. It was proposed that the same hydrogen, when diffused to the silicon-silicon dioxide interface, gave rise to the slow states and turn-around effect^{9,10}. Weinberg *et al.* had studied the generation of positive charge under vacuum ultra-violet light (VUV) and proposed that exciton transport might be responsible for the positive charge¹¹. In a subsequent experiment, they observed an enhancement of positive charge generation in a wet oxide and proposed that hydrogen might be an alternative explanation for their observation¹². In the same experiments, it was shown that the positive charge observed had charging and discharging behavior similar to that of slow states generated by electron trapping¹³.

So far, most of the results on interface effects and turn-around effect were obtained on structures with aluminum gates. When structures with polysilicon gates were examined, they showed much lower density of electron trapping and significantly reduced interface effects². It was proposed that the high temperature processes required for the preparation of polysilicon reduced the density of water-related centers in the oxide². The effect was equivalent to the high temperature anneal experiments reported previously⁶. The use of gate metals other than aluminum or polysilicon were not investigated. In the present work, the use of gold and titanium as alternative gate metals was

explored. Very different results were obtained, showing that the turn-around effect might be related to the use of aluminum.

In the present experiments, HCl oxides, dry oxides and water-diffused¹⁰ oxides were used, with thicknesses from 48 nm to 56 nm. In a set of HCl oxides, either 500 nm aluminum or 500 nm aluminum/100 nm titanium (with titanium in contact with the oxide) in 32 mil diameter dots were used as top electrodes. In a set of water-diffused oxides, 30 nm of gold or 400 nm of aluminum were used. The wafers were P type, boron doped, 0.1 to 0.2 Ω-cm in resistivity and <100> in orientation. The systems for avalanche injection and flatband voltage tracking has been reported earlier⁵. The experiment was carried out in a probe station which could be heated to 250°C. The probe station was filled with dry nitrogen during the course of the experiment.

The results of the experiment are summarized in figures 1 and 2. In figure 1, the flatband voltage shifts as a function of injected charge were plotted for aluminum and aluminum/titanium gate capacitors at room temperature and 120°C. The results for aluminum gates were similar to those reported earlier². At room temperature, the turn-around effect was observed with the flatband voltage shift going negative. A normal trapping curve was obtained for 120°C. This is because at elevated temperatures, it is possible for the silicon surface region to communicate better with the slow states to minimize the anomalous positive charge⁵. The flatband voltage shift curve at the high temperature was basically the curve due to bulk electron trapping. Also

shown in figure 1 were the results for aluminum/titanium gates. The difference was very significant. First of all, a very small turn-around effect was observed at the room temperature. Secondly, the change in the curves from room temperature to 120°C was much smaller compared to the ones with aluminum gates. The 120°C results for aluminum and aluminum/titanium were slightly different but in terms of the density of electron traps, they were within ten percent of each other. The difference was too small to explain the big difference in the turn-around effect at room temperature.

Figure 2 showed the curves for aluminum and gold electrodes. The results for aluminum gate were similar to figure 1 except for the fact that the curve at room temperature did not go negative. The results for gold were more interesting. There was actually a larger turn-around effect at 120°C compared to room temperature. This is totally different from the results for aluminum and aluminum/titanium electrodes. But still, the important point is that the densities of electron traps for aluminum and gold electrodes were within ten percent of each other. The difference was not sufficient to explain the difference in the turn-around effect.

The above results do not prove or disprove the two models proposed earlier to explain the turn-around effect. However, the present results seem to indicate that aluminum is an important component in the effect. It is possible that there are species generated by the reaction of aluminum with silicon dioxide during deposition that are released by the passage of electrons. Anoth-

er possibility is that aluminum may catalyze the liberation of hydrogen after electron trapping. The present results might also explain why significant turn-around effect was not observed in oxides that were nitridized in ammonia¹⁴. If there was indeed an oxynitride layer formed at the outer interface, such a layer, being a good diffusion barrier, might minimize the reaction between the aluminum and silicon dioxide. In conclusion, it was observed that when aluminum/titanium or gold was used instead of aluminum for the gate, the generation of positive charge at the silicon-silicon dioxide after electron trapping was significantly reduced. The results may account for the different results reported by different workers using either aluminum or polysilicon gates. Much more work has to be performed to understand the turn-around effect.

ACKNOWLEDGEMENT

The authors would like to thank J.M. Aitken, whose work inspired the present experiment, D.R. Young and D.J. DiMaria for very valuable discussions on electron trapping. The technical support and sample preparation by J.A. Calise and the Silicon Processing Facility, and the gold deposition by J. Kirtley are greatly appreciated. He would also like to thank D.R. Young and M.H. Brodsky for a critical reading of the manuscript. This work was sponsored by the Defense Advance Research Projects Agency (DoD) ARPA Order No. 4012 under Contract No. MDA903-81-C-0100 issued by Department of Army, Defense Supply Service-Washington, Washington, DC 20310.

REFERENCES

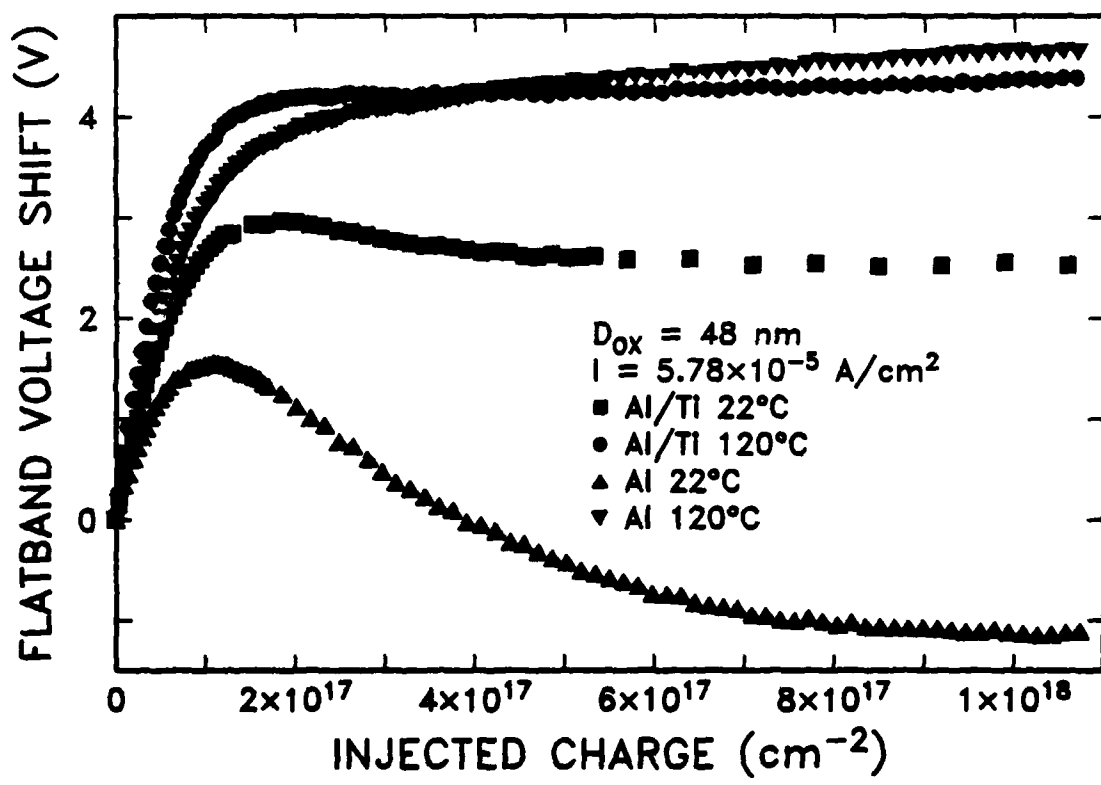
1. R.A. Gdula, J. Electrochem. Soc., **123**, 42 (1976)
2. D.R. Young, E.A. Irene, D.J. DiMaria, R.F. DeKeersmaecker and H.Z. Massoud, J. Appl. Phys., **50**, 6366 (1979)
3. M.V. Fischetti, R. Gastaldi, F. Maggioni and A. Modelli, J. Appl. Phys., **53**, 3129 (1982)
4. M.V. Fischetti, R. Gastaldi, F. Maggioni and A. Modelli, J. Appl. Phys., **53**, 3136 (1982)
5. S.K. Lai and D.R. Young, J. Appl. Phys., **52**, 6231 (1981)
6. S.K. Lai, D.R. Young, J.A. Calise and F.J. Feigl, J. Appl. Phys., **52**, 5691 (1981)
7. S. Pang, S.A. Lyon and W.C. Johnson, Appl. Phys. Lett. **40**, 709 (1982)
8. E.H. Nicollian, C.N. Berglund, P.F. Schmidt, and J.M. Andrews, J. Appl. Phys. **42**, 5654 (1971).
9. D.R. Young (private communication)
10. F.J. Feigl, D.R. Young, D.J. DiMaria, S.K. Lai and J.A. Calise, J. Appl. Phys., **52**, 5665 (1981)

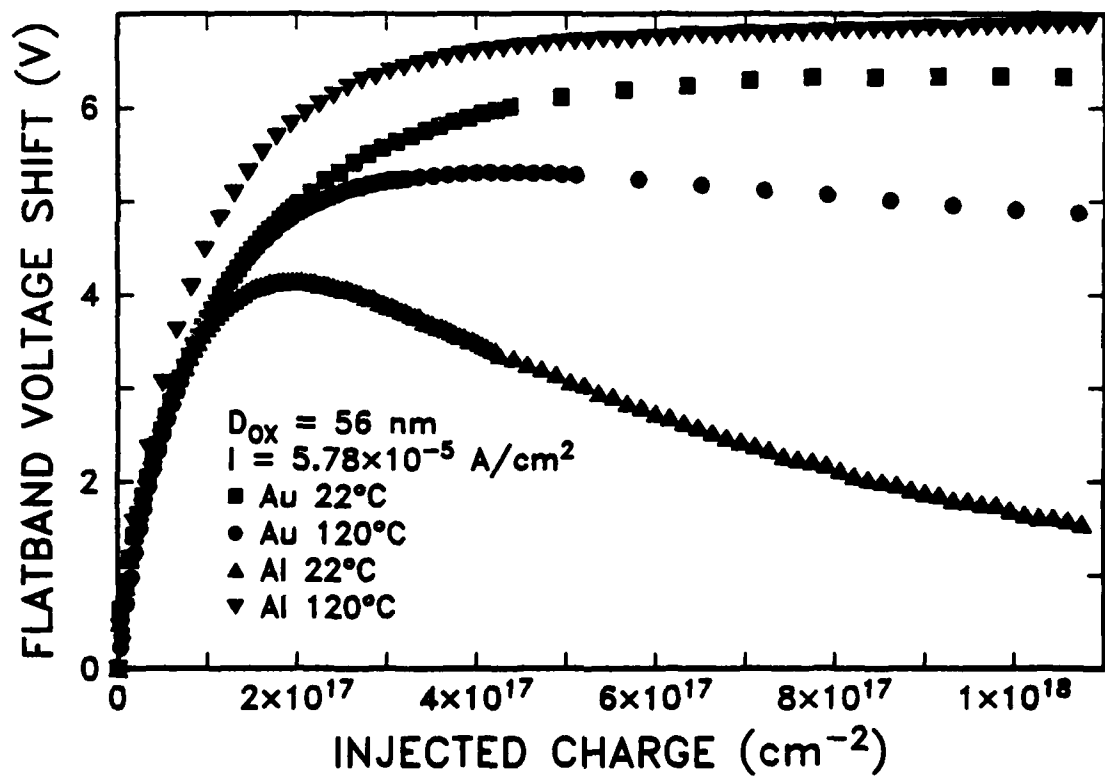
11. Z.A. Weinberg and G.W. Rubloff, *Appl. Phys. Lett.*, **32**, 184 (1978)
12. Z.A. Weinberg, D.R. Young, D.J. DiMaria and G.W. Rubloff, *J. Appl. Phys.*, **50**, 5757 (1979)
13. D.R. Young (unpublished results)
14. S.K. Lai, D.W. Dong and A. Hartstein, (accepted by *J. of Electrochem. Soc.*)

FIGURE CAPTIONS

Figure 1 Flatband voltage shifts as a function of injected charge at room temperature and 120°C for oxides with aluminum or aluminum/titanium as top electrodes.

Figure 2 Flatband voltage shifts as a function of injected charge at room temperature and 120°C for an oxide with gold or aluminum as top electrodes.





Extended Cyclability in Electrically-Alterable Read-Only-Memories*

D.J. DiMaria, D.W. Dong and C. Falcony^(a)
I.B.M. Thomas J. Watson Research Center
Yorktown Heights, New York 10598

and

S.R. Brorson
Massachusetts Institute of Technology
Cambridge, Massachusetts 02139

Typed by Stella B. Havreluk (3277)

Abstract: An electrically-alterable read-only-memory using silicon dioxide and silicon-rich silicon dioxide layers capable of being cycled $\geq 10^7$ times by minimizing electron charge trapping in the SiO₂ layers of the device by incorporation of small amounts of silicon is reported for the first time. Charge transfer to and from a floating poly-crystalline silicon layer from a control gate electrode is accomplished by means of a modified dual-electron-injector-structure stack. This modified stack has the intervening silicon dioxide layer, which is sandwiched between silicon-rich silicon dioxide injectors, replaced by a slightly off-stoichiometric oxide containing between 1% and 6% excess atomic silicon above the normal 33% found in silicon dioxide. A brief discussion of a physical model which is believed to account for the observed phenomenon is given.

***Sponsored by Defense Advanced Research Projects Agency (DoD) ARPA Order No. 4012
Under Contract No. MDA903-81-C-0100 issued by Department of Army, Defense Supply
Service-Washington, Washington, DC 20310**

**(a) Sponsored in part by Consejo Nacional de Ciencia y Tecnología (CONACyT) and Centro de
Investigaciones y Estudios Avanzados del I.P.N. (CIEA), Mexico.**

The cyclability (that is, the number of write/erase cycles) of electrically-alterable read-only-memories (EAROMs), using SiO_2 layers for transferring charge to or from a storage layer, is limited by electron charge trapping in the SiO_2 layers [1-4]. This charge trapping occurs in sites situated 4-5 eV deep from the bottom of the conduction band edge in the ≈ 9 eV forbidden bandgap of SiO_2 [5]. These sites are believed to be related to H_2O and OH impurities bonded to Si [6]. Furthermore, it has been shown that these impurities, and therefore the electron trapping associated with them, can be reduced by extended high temperature annealing [4,6,7]. However, the improvement in cyclability is usually only one or two orders of magnitude [4]. Cyclability of these EAROMs is ultimately limited to $\lesssim 10^6$ cycles by electron traps with very small capture cross sections ($\lesssim 10^{-19} \text{ cm}^2$) which seem to have no relationship to water incorporation into the SiO_2 layers during processing [8]. Clearly, to extend the cyclability of EAROMs into a range ($\gtrsim 10^{10}$ cycles) where they can function as non-volatile random-access-memories (NVRAMs) a new material other than SiO_2 is needed. It is the purpose of this letter to describe the use of such a material, which is formed from a slightly Si-rich off-stoichiometric SiO_2 layer, in EAROM type devices.

The basic EAROM device used in this study is shown schematically in Fig. 1. It is composed of an n-type degeneratively doped floating poly-crystalline silicon (poly-Si) storage layer and a modified dual-electron-injector-structure (DEIS) stack [1,4,9,10] which is used to charge or discharge the floating poly-Si layer with electrons. The DEIS EAROM has been recently discussed in the literature [1,4,9,10] and will not be described here. The modification of the DEIS stack is the use of a slightly off-stoichiometric chemically-vapor-deposited (CVD) SiO_2 layer with ≈ 1 to 6% excess atomic Si as a replacement for the normally stoichiometric intervening SiO_2 layer. The Si-rich SiO_2 injectors of the DEIS stack which sandwich this modified layer (see Fig. 1) still contain $\gtrsim 13\%$ excess atomic Si as has been reported previously [1,9,11]. The fabrication procedure for the device shown in Fig. 1 is very similar to the poly-Si gate process previously reported [1,9] except that an extra masking step has been added to make the control poly-Si gate smaller than the floating poly-Si gate with areas of $1.3 \times 10^{-6} \text{ cm}^2$ and $2.5 \times 10^{-6} \text{ cm}^2$, respectively, at the masking level. The unequal gate areas were used to increase the electric field magnitude across the DEIS stack with respect to the field across the gate oxide which separates the floating poly-Si layer from the Si substrate. In Figs. 2-4, R_o is the ratio of the concentration of N_2O to SiH_4 in the gas phase during CVD deposition [1-3,4,9-11], and it is used as an indicator of the Si content of the SiO_2 layer of the DEIS. $R_o \gtrsim 100$ implies that this layer is 33% atomic Si in composition (that is, stoichiometric SiO_2), while $R_o < 100$ implies the oxide has excess Si in it. $R_o = 50$ to $R_o = 30$ correspond to $\approx 1\%$ to $\approx 6\%$ excess atomic Si, respectively. The threshold voltages of the devices

after being written or erased were determined from measurements of the channel conductance as described previously [1,9,10].

The main conclusion from this work is shown in Fig. 2 where DEIS EAROMs with the normal stoichiometric SiO_2 layers are compared to identical devices with the exception that the intervening SiO_2 layer of the DEIS stack contains $\approx 1\%$ to $\approx 6\%$ excess atomic Si. These figures show an increase in the cyclability of at least 10^4 orders of magnitude before threshold voltage window collapse starts due to charge trapping [1-4] in the modified DEIS EAROMs compared to the normal oxide structures.

The threshold voltage window collapse in the normal oxide structures of Fig. 2 has been accelerated by design to emphasize this result. This is achieved by using thicker intervening SiO_2 layers (300 \AA in Fig. 2) than used in devices reported in previous publications [1,4,9,10] to get more bulk SiO_2 electron trapping [1-4]. This is apparent if the rate of threshold voltage window collapse as a function of oxide thickness on the normal DEIS EAROMs is compared for SiO_2 thicknesses in the range from 100 \AA to 600 \AA [4]. Figure 2 shows that adding more Si (up to $\approx 6\%$ excess atomic Si) to the modified intervening SiO_2 layer of the DEIS gives even a larger number of cycles. Currently, on a device similar to one of those in Fig. 2 with an $R_o = 30$ off-stoichiometric SiO_2 layer 600 \AA in thickness, 3.5×10^{10} cycles have been achieved with a 60% reduction in the value of the threshold voltage window which was initially set at $\approx 6 \text{ V}$.

Increasing the Si content of the intervening oxide layer of the DEIS will be ultimately limited by the degradation in the retention of the device; that is, charge leakage off of or on to the floating gate storage electrode. Figure 3 shows the retention characteristics at room temperature for a grounded control gate condition for the same series of devices as in Fig. 2 after the floating poly-Si layer had been charged from a virgin as-fabricated state with electrons to produce a threshold voltage of $\approx +6\text{-}7 \text{ V}$. Over a 24 hr. period the DEIS stack with $\approx 2\text{-}3\%$ excess atomic Si in the intervening 600 \AA thick oxide layer has the same retention characteristic as the control structure with the stoichiometric 300 \AA thick intervening SiO_2 layer. As seen in Fig. 3, adding more Si to the intervening oxide layer does degrade the retention somewhat, as expected. Other DEIS stacks with 1-2% excess atomic Si in a 300 \AA thick intervening oxide layer also showed the same retention characteristic as the control structure in Fig. 3. Observations concerning the retention degradation similar to those in Fig. 2 were seen on devices from the same wafers as in Fig. 2 when electrons were removed from the floating gate, leaving the devices with a threshold voltage of $\approx 1.5 \text{ V}$ initially. Clearly, there is a trade-off with these devices between the maximum number of

cycles attainable and long term charge retention due to the added conductivity of the off-stoichiometric intervening oxide layers. Measurements of the retention characteristics on the devices in Figs. 2-3 after cycling to at least 10^7 cycles produced results similar to those in Fig. 3 indicating no degradation of the material in the DEIS stack. Fig. 4 demonstrates this point for a device similar to one of those in Figs. 2 and 3 with a 600 Å thick off-stoichiometric intervening oxide with 5-6% excess atomic Si ($R_o=30$) in it which was cycled out to 4.3×10^9 cycles and had its retention characteristic measured periodically after various amounts of cycling. Degradation phenomenon in retention characteristic has been observed in EROM structures employing Si_3N_4 layers, usually called metal-nitride-oxide-silicon (MNOS) devices [12].

The modified DEIS devices have been observed to operate more symmetrically at lower voltages than corresponding control structures with stoichiometric intervening SiO_2 layers for write/erase pulse times $\gtrsim 1$ msec. However, for write/erase pulse times $\lesssim 1$ msec, these modified devices require larger voltages for the write or erase operation compared to control structures. This observation is believed to be due to differences in the conduction mechanisms (i.e., the current vs. voltage characteristics) in the different DEIS stacks (with intervening SiO_2 or off-stoichiometric oxide layers) which control the write/erase operation. Also, the write/erase operation of the full DEIS stack with the intervening off-stoichiometric SiO_2 layer and both top and bottom Si-rich SiO_2 injectors has been observed to occur at lower gate voltages than equivalent devices with no top or bottom injectors.

The physical details of the conductivity of the intervening oxide layer of the DEIS stack accounts for the improvements of the modified stack with the off-stoichiometric oxide layer. Although the physics of this conduction mechanism will be discussed in detail in a future publication [13], the main aspects will be summarized here. The Si-rich SiO_2 injector interface with stoichiometric SiO_2 is believed to provide localized electric field enhancement due to the curvature of Si islands at this interface which accounts for the observed high current injection (via a Fowler-Nordheim tunneling mechanism) at moderate average electric field strengths [1,2,4,9-11]. These tunneling electrons still must penetrate an ≈ 3 eV energy barrier at this interface to get into the SiO_2 conduction band as "free" electrons. One out of every 10^3 to 10^7 of these "free" conduction band electrons (depending on processing) can be captured by the deep trapping sites in forbidden bandgap of the SiO_2 which are 4-5 eV deep from the bottom of the oxide conduction band [3,6-8] which eventually leads to the threshold voltage window collapse observed in the control structures in Figs. 2 and 3. By adding small amounts of Si to the intervening SiO_2 layer, small localized Si regions (similar to those seen in the Si-rich SiO_2 injectors [1,14-15]) are formed [13] which are believed to allow another type

of carrier injection into this layer of the DEIS. This injection mechanism is by direct tunneling from the larger interfacial islands of Si ($\leq 50 \text{ \AA}$ in size) in the injector region to the smaller islands of Si (probably $\leq 20 \text{ \AA}$ in size [13]) in the off-stoichiometric SiO_2 layer. These injected carriers (which could also include holes) could move from Si island to Si island by direct tunneling in the intervening oxide layer of the DEIS until they reach the opposite injector-oxide interface. Electron capture into deep trapping sites under this type of conduction mechanism would not be expected to be similar to that for "free" electron capture from the SiO_2 conduction band. The fact that any electron capture occurs at all in these off-stoichiometric oxide materials suggests that a component of the injected electrons still has a finite probability of getting into a "free" SiO_2 conduction band state, and/or that the probability of capturing a tunneling electron is very small, and/or that some fraction of tunneling holes (if present) can annihilate trapped electrons. Additionally, electrons captured into the deep SiO_2 states would also have a finite probability of directly tunneling under energetically favorable conditions (which are probably strongly influenced by the electric fields in off-stoichiometric oxide layer) to the small Si islands in the off-stoichiometric SiO_2 .

This letter has reported some of the initial observations of a large improvement in cyclability of DEIS EAROMs by the addition of a small amount of Si to the normally stoichiometric intervening SiO_2 layer of the DEIS stack. Devices reported here have been shown capable of achieving $\gtrsim 10^7$ cycles with some degradation in the charge retention of the floating gate electrode. The possibility of achieving even more write/erase cycles with lower voltages and faster switching speeds by using thinner layers and/or more Si incorporation is currently under investigation and will be reported in the future.

The authors would like to acknowledge helpful discussions on inelastic tunneling with J.R. Kirtley and T.N. Theis, the critical reading of this manuscript by D.R. Young and M.H. Brodsky, the technical assistance of F.L. Pesavento, and the device fabrication by the silicon processing group at the T.J. Watson Research Center (in particular, E.P. Gabriel, E.J. Petrillo, and D.L. Quinlan). This research was supported in part by the Defense Advanced Research Projects Agency (DoD) ARPA Order No. 4012, under Contract No. MDA903-81-C-010 issued by the Department of the Army, Defense Supply Service-Washington, Washington, D.C. 20310.

References

- Sponsored by Defense Advanced Research Projects Agency (DoD) ARPA Order No. 4012 Under Contract No. MDA903-81-C-0100 issued by Department of Army, Defense Supply Service-Washington, Washington, DC 20310
- (a) Sponsored in part by Consejo Nacional de Ciencia y Technologia (CONACyT) and Centro de Investigaciones y Estudios Avanzados del I.P.N. (CIEA), Mexico.
- 1. D.J. DiMaria, K.M. DeMeyer, C.M. Serrano, and D.W. Dong, J. Appl. Phys. 52, 4825 (1981).
- 2. D.J. DiMaria, R. Ghez, and D.W. Dong, J. Appl. Phys. 51, 4830 (1980).
- 3. F.J. Feigl, D.R. Young, D.J. DiMaria, S. Lai, and J. Calise, J. Appl. Phys. 52, 5665 (1981).
- 4. C. Falcony, D.J. DiMaria, D.W. Dong, and K.M. DeMeyer, J. Appl. Phys. (January 1982).
- 5. D.D. Rathman, F.J. Feigl, and S.R. Butler, in Insulating Films on Semiconductors, edited by G. Roberts (Institute of Physics and Physical Society, London, 1980), p. 48.
- 6. A.M. Hartstein and D.R. Young, Appl. Phys. Lett. 38, 631 (1981).
- 7. S.K. Lai, D.R. Young, J.A. Calise, and F.J. Feigl, J. Appl. Phys. 52, 5691 (1981).
- 8. D.R. Young, J. Appl. Phys. 52, 4090 (1981).
- 9. D.J. DiMaria, K.M. DeMeyer, and D.W. Dong, IEEE Electron Device Lett. EDL-1, 179 (1980).
- 10. D.J. DiMaria, K.M. DeMeyer, and D.W. Dong, IEEE Trans. on Electron Devices ED-28, 1047 (1981).
- 11. D.J. DiMaria and D.W. Dong, J. Appl. Phys. 51, 2722 (1980).
- 12. M.H. White, J.W. Dzimianski, and M.C. Peekerar, IEEE Trans. on Electron Devices ED-24, 577 (1977).

13. C. Falcony, D.J. DiMaria, D.W. Dong, J.R. Kirtley, T.N. Theis, J.C. Tsang, and S.R. Brorson, *Unpublished*.
14. M. Hamasaki, T. Adachi, S. Wakayama, and M. Kikuchi, *J. Appl. Phys.* 49, 3987 (1978).
15. A. Hartstein, J.C. Tsang, D.J. DiMaria, and D.W. Dong, *Appl. Phys. Lett.* 36, 836 (1980).

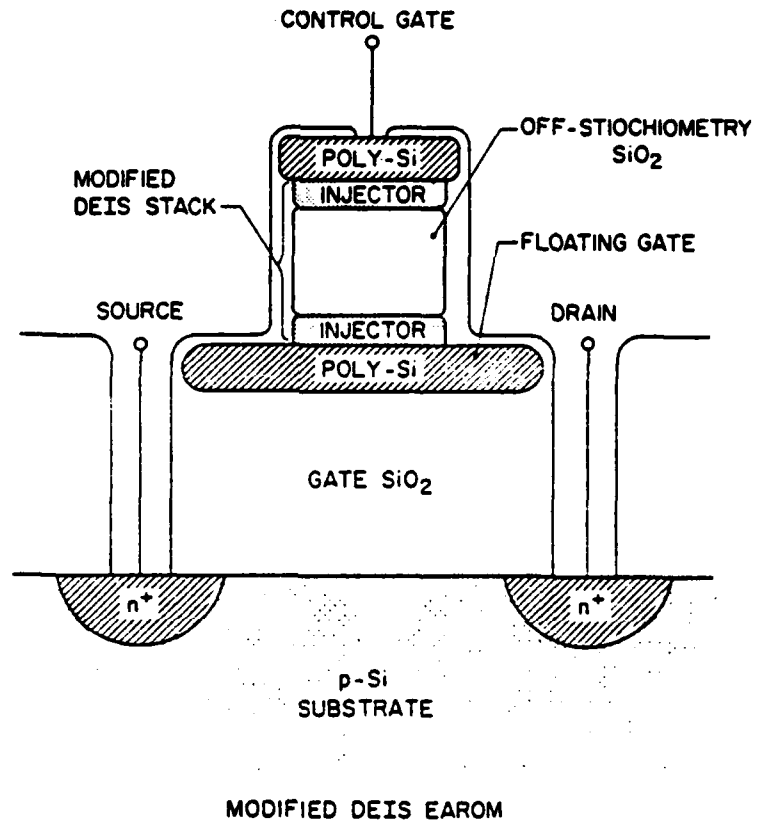


Figure 1. Schematic representation of a three port modified DEIS EAROM with an off-stoichiometric intervening oxide layer in the DEIS stack. Not drawn to scale.

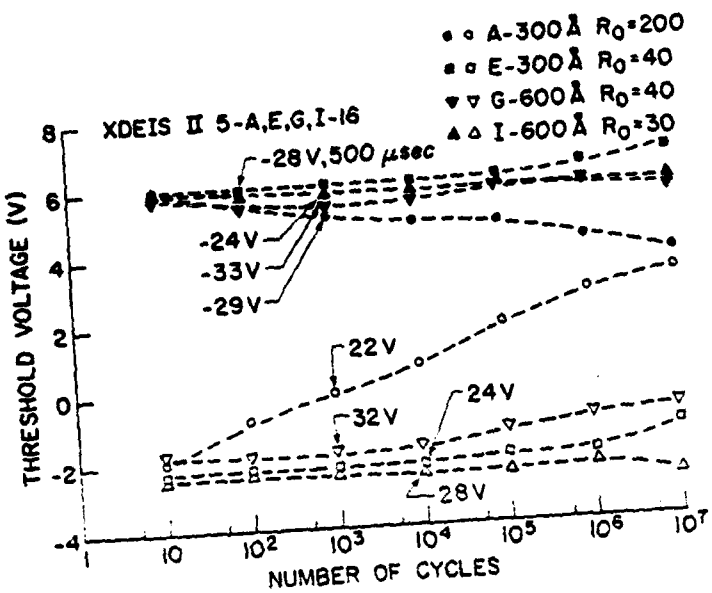


Figure 2. Threshold voltage after write or erase operation as a function of the number of write/erase cycles on devices from the XDEIS II-5 series of samples. Wafer A is a control with the normal stoichiometric oxide (300 Å in thickness) in the DEIS stack, while wafers E, G, and I have modified DEIS stacks with off-stoichiometric oxides 300 Å or 600 Å in thickness containing \approx 3-6% excess atomic Si for $R_o=40$ to 30 in the intervening oxide of the DEIS as described in the text. The Si-rich SiO_2 injectors were each 200 Å in thickness and contained \geq 13% excess atomic Si and the gate oxide was 660 Å in thickness. The control gate and floating gates had areas of $1.3 \times 10^{-6} \text{ cm}^2$ and $2.5 \times 10^{-6} \text{ cm}^2$, respectively, at the masking level.

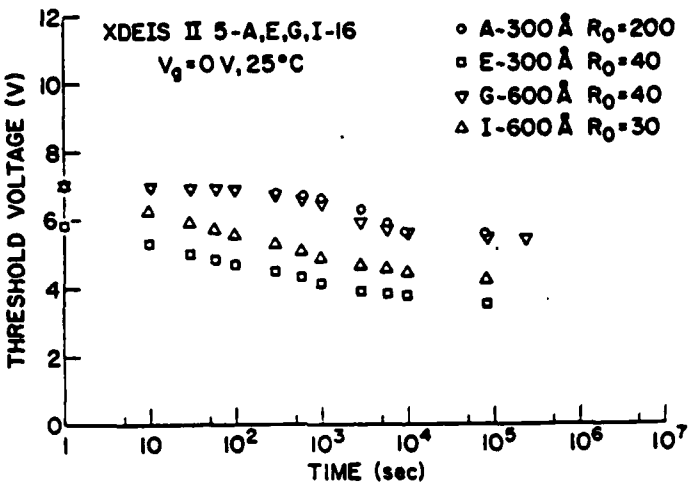


Figure 3. Retention data (threshold voltage as a function of time) on the same series of samples as in Fig. 2 after the devices were charged from a virgin as-fabricated state to an initial threshold voltage of $\approx 6\text{-}7$ V.

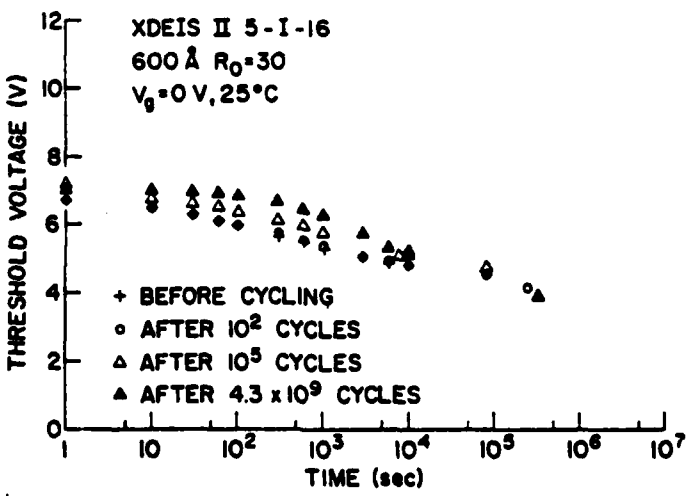


Figure 4. Retention data (threshold voltage as a function of time) on a device from wafer XDEISII-5-I which has a 600 Å thick off-stoichiometric oxide with $R_0=30$ in the DEIS stack of the EAROM. Devices were charged from either a virgin as-fabricated state or cycled state, as indicated, to an initial threshold voltage of ≈ 7 V.

**A NEW LOW-VOLTAGE Si-COMPATIBLE
ELECTROLUMINESCENT DEVICE***

D. J. Robbins^(a), C. Falcony^(b), D. J. DiMaria, D. W. Dong

J. F. DeGelormo, I. F. Chang and D. B. Dove

IBM T.J. Watson Research Center

P. O. Box 218

Yorktown Heights, NY 10598

ABSTRACT

Thin film direct-current electroluminescent devices with ZnS:Mn as the active light-emitting layer have been fabricated on Si wafers. The devices incorporate a high-efficiency electron injector layer capable of passing high current densities ($> 10^{-2} \text{ A cm}^{-2}$ DC) through the active layer. A useful luminance of 78 fL has been achieved at 48V, i.e. at significantly lower voltage than for conventional AC thin film or DC powder electroluminescent devices. The structure also includes a potential energy step at the interface between SiO_2 and ZnS due to the difference in electron affinities which offers the possibility of hot electron injection into the active layer. The unique combination of efficient cathode emission and hot injection possible in these devices suggests that a solid state analogue of the cathode ray tube may be realizable.

* Sponsored in part by Defense Advanced Research Projects Agency (DoD) ARPA Order No. 4012 Under Contract No. MDA903-81-C-0100 issued by Department of Army, Defense Supply Service-Washington, Washington, DC 20310.

(a) On leave from: Royal Signals and Radar Establishment, Malvern, England.

(b) Sponsored in part by Consejo Nacional de Ciencia y Technologia (CONACyT) and Centro de Investigaciones y Estudios Avanzados del I.P.N. (CIEA), Mexico.

Large area, high field electroluminescence (EL) continues to be an active area of display research.^{1,2} In recent years the most widely investigated technology has been that of AC thin film electroluminescence (ACTFEL), using Mn²⁺-activated ZnS as a light-emitting layer sandwiched between two dielectric layers of high breakdown strength.³ Structures of this kind can produce devices with good brightness stability, but the capacitive coupling necessitates high voltage AC drive waveforms (typically >100V rms) which in turn require relatively high cost customized driving circuitry. From this point of view low voltage DC electroluminescence (DCEL) has many attractions. Powder DCEL cells have been developed,⁴ but these still operate at relatively high voltage (typically ~100V) and also require electrical forming of the active layer. Attempts to produce DC thin film electroluminescence (DCTFEL) devices have met with the fundamental problem of controlling current flow and preventing the catastrophic breakdown associated with current runaway. Several approaches to the control of current injection into the active ZnS:Mn layer have been tried, including tunnel injection in reverse-biased Schottky diodes⁵ and in heterojunctions formed electrically⁶ or during growth,^{7,8} and the use of series resistive layers.⁹ However thus far no DCTFEL technology has emerged which combines low voltage operation, reproducible electrical characteristics, large area compatibility and long-term stability. The development of such a technology remains a major goal in display research.

Here we report a low voltage, Si-compatible DCTFEL structure potentially suited to the production of integrated flat panel displays. The structure incorporates a high-efficiency electron injector layer, viz. (Si-rich SiO₂)-SiO₂, originally developed for application in electrically-alterable read-only-memory (EAROM) devices,¹⁰ and used here for the first time in a display device. Prototype devices, illustrated in Figure 1(a), have been fabricated on 1.25-inch Si wafers. The Si-rich SiO₂ and SiO₂ layers were made by a chemical vapour deposition (CVD) process.¹¹ A 1.5 cm x 1.5 cm ZnS:Mn layer was deposited in the centre of the wafer by e-beam evaporation through a mask, followed by post-growth annealing. The Mn:Zn mole ratio determined by X-ray fluorescence was typically ~0.005. A 10 x 10 matrix

of 1.25 mm diameter, semi-transparent indium-tin oxide (ITO) electrodes on 3.1 mm centres was finally deposited to define each device area; these ITO contacts will be referred to as the 'gate' electrodes. A feature of this structure is that some of the gate electrodes are deposited directly onto the SiO_2 layer, generating 'control' devices which are useful for electrical characterization of the injector layer itself.

The energy level diagram for these devices, with the gate biased positively, is illustrated schematically in Figure 1(b). Electron injection is controlled by tunneling from the n-type Si substrate into the small ($\leq 50 \text{ \AA}$ diameter) Si islands in the Si-rich SiO_2 layer¹⁰, represented as potential wells in Figure 1(b). At sufficiently high fields electrons can move readily through the Si-rich SiO_2 layer to the interface with the SiO_2 layer. There they are injected from the last layer of Si islands into the conduction band (CB) of the SiO_2 via a field-enhanced Fowler-Nordheim tunneling mechanism,¹⁰ which is the rate-limiting step in the current flow. After crossing the SiO_2 layer the electrons are injected into the active layer at the $\text{SiO}_2\text{-ZnS:Mn}$ interface. A detailed analysis of the device properties, to be reported elsewhere,¹² shows that the Mn^{2+} impurity centres are excited to emit their characteristic yellow ($\sim 580 \text{ nm}$) luminescence by direct excitation involving a hot electron distribution in the active ZnS:Mn layer.

The use of the two-phase Si-rich SiO_2 layer to control current injection has two major advantages over a conventional semiconductor-insulator interface, both of which are illustrated in Figure 2. First, high current densities can be passed through the insulating SiO_2 and ZnS:Mn layers, in the range $10^{-2} \text{ A cm}^{-2}$ DC to $\sim 10^2 \text{ A cm}^{-2}$ under short voltage pulses. However, because of the field enhancement at the surface of the irregular Si islands the Fowler-Nordheim tunnel injection occurs at significantly lower average fields than is the case for a planar Si/ SiO_2 interface.¹⁰ Curve A in Figure 2 is the I-V characteristic under forward (positive gate) bias for a control device on wafer 15N-5 which has no Si-rich SiO_2 layer; i.e. the SiO_2 is deposited directly onto the Si substrate and the gate deposited directly on the SiO_2 . These I-V characteristics were measured using a voltage source ramped at a constant rate of

0.5 V sec⁻¹ from zero. The constant-current portion of the curves is a measure of the capacitance of the structure i.e. $I_d = C dV/dt$. The threshold for real current injection (i.e. for current $> I_d$) is observed to be ~ 27 V, corresponding to an average field of $\sim 5.4 \times 10^6$ V cm⁻¹ in the oxide layer. Curve C is a similar characteristic for a control device on wafer 9L-14 which has the standard injector layer. In this case the threshold is ~ 10 V, corresponding to an average field $\sim 2 \times 10^6$ V cm⁻¹ in the oxide. Curves B and D are forward bias I-V characteristics for wafers 15N-5 and 9L-14 (without and with the injector layer respectively), but now including the ZnS:Mn layer. For a fixed voltage ramp rate the average field in the active layer at a particular current is given by the voltage difference between the I-V characteristics for the control and ZnS devices on a wafer [i.e. ΔV (A-B) and $\Delta V'$ (C-D) in Figure 2], divided by the ZnS thickness. At a current of 3×10^{-9} A the average field in the ZnS:Mn layer for both wafers is $\sim 0.6 \times 10^6$ V cm⁻¹. Curve E in Figure 2 is the I-V characteristic for a ZnS device on wafer 9L-14 under reverse (negative gate) bias. Under reverse bias the Si-rich SiO₂ injector layer plays no part in controlling current flow through the insulators and the I-V behaviour is determined by tunneling at the highest barrier, which occurs in this case at the ZnS/SiO₂ interface. The closeness of the electron affinities of ZnS (3.9 eV) and Si (4.0 eV) produces comparable barrier heights at the ZnS/SiO₂ (~ 3.0 eV) and Si/SiO₂ (~ 3.1 eV) interfaces. This is the reason for the similarity of the reverse bias curve E in Figure 2 to curve B, i.e. to a device under forward bias with a similar ZnS layer but with no injector layer.

The second major advantage of the injector layer is that it provides screening against low field breakdown of the structure.¹⁰ Curve A in Figure 2 shows evidence of current noise associated with local field variation at irregularities on the Si/SiO₂ interface, leading to catastrophic breakdown at a current density of $\sim 3 \times 10^{-6}$ A cm⁻². Devices incorporating the Si-rich SiO₂ injector, on the other hand, can be reversibly cycled to current densities of $\sim 10^{-2}$ A cm⁻², as illustrated by curve C. In this case the negative space charge in the Si islands tends to screen out any local field variation at the Si interface, producing a macroscopically uniform current injection and preventing current runaway.^{10,13} The hysteresis in the I-V characteris-

tics shown in Figure 2 arises from electron trapping in the SiO_2 layer.¹³ This charge trapping can lead to instabilities and represents a limitation of the present devices.

A further feature of these devices is illustrated by the energy level diagram in Figure 1(b). The electron affinity difference between SiO_2 (0.9 eV) and ZnS (3.9 eV) generates a potential energy step of ~ 3 eV at the SiO_2/ZnS interface. In principle this step may allow hot electron injection into the ZnS:Mn layer, offering the possibility of higher energy conversion efficiency than can be achieved for example in conventional ACTFEL devices where excited electrons are generated by field ionization of impurity or interface levels.¹⁴ The advantage of hot injection into the luminescent layer has been discussed by Morton and Williams¹⁵ for a structure in which the processes of electron heating and light generation are spatially separated. However the EL structure described here represents the first display device in which the possibility of hot electron injection due to a potential energy step at an insulator/ZnS junction has been clearly proposed.

Typical I-V and corresponding light output-voltage (B-V) curves are shown in Figures 3(a) and 3(b) for different device locations on the 10 x 10 gate electrode matrix of wafer 9L-14. Luminance measured with a calibrated spot photometer at various device currents is listed in Table 1. The calculated luminous efficiencies quoted in Table 1 are external efficiencies for the device which make no correction for light extraction or optical transmission factors in the thin film structure. They therefore represent a lower limit for the device efficiency. The voltages at a given current level are higher in Table 1 than in the ramp I-V data of Figure 3(a). This is because the luminance measurements were made under conditions of fixed current over a period of time appreciably longer than the ramp time, when the I-V curve is displaced by charge trapping effects.

Two points should be made from the data in Figure 3. First, from curves 3 the light output vs current relationship in the current range $10^{-9} - 10^{-4}$ A has the form $B \propto I^n$, where n takes a value close to, but slightly greater than, unity; the luminescence quantum efficiency $\eta_q \propto B/I$ therefore shows only a small variation over this current range. At the same time the

average field in the ZnS layer increases from $\sim 0.55 \times 10^6 \text{ V cm}^{-1}$ to $\sim 0.90 \times 10^6 \text{ V cm}^{-1}$. Therefore η_q , which depends upon the hot electron distribution in the ZnS layer, is not a sensitive function of average electric field in this range. Secondly comparison of curves 4 and 5, which are forward and reverse characteristics for the same gate electrode, shows that the quantum efficiencies are similar for the two bias directions although the power efficiency is significantly less under reverse bias. It should be said that this is not always the case since we have observed that, while all devices with injector layers behave in a similar way under forward bias, η_q can often be appreciably lower under reverse bias. However the fact that some devices show similar η_q values in both forward and reverse direction is strong evidence that hot electron injection at the SiO_2/ZnS interface is not a significant factor in determining efficiency, since hot injection at the potential step could occur only under forward bias. The efficiency in the present devices is set by field and space charge distributions in the SiO_2 and ZnS layers.¹² On the other hand it is possible that the absence of hot injection effects results from poor quality of the ZnS phosphor material near the SiO_2 interface, and that improvements in material deposition technology may lead to higher device efficiencies.

The luminous efficiencies listed in Table 1 compare very favorably with other EL technologies. External efficiencies ~ 0.5 lumens per Watt (1 W^{-1}) are typically observed in ACTFEL, although values of $1\text{-}8 \text{ l W}^{-1}$ have been quoted.² Powder DCEL cells,² and DCTFEL structures incorporating cermet series resistance layers⁹ or graded alloy insulators,¹⁶ have efficiencies in the range $0.1\text{-}0.4 \text{ l W}^{-1}$. The efficiencies of ZnSe:Mn/GaAs heterojunction^{7,8} and ZnS:Mn Schottky diode¹⁷ devices are at least an order of magnitude lower. The decrease in luminous efficiency at higher currents evident in Table 1 is not entirely a true saturation of the light output. It is due in part to an increase in voltage necessary to compensate for charge trapping, and in part to a transient reduction in luminescence efficiency which correlates with an increase in the rate of positive space charge accumulation in the ZnS layer.¹² This transient effect can be reversed over a period of several minutes under constant current drive at 10^{-4}A . Finally, it should be noted that the lower limit to the conversion

efficiency of the ZnS:Mn layer itself is ~ 2.5 times greater than the overall values listed in Table 1, since only ~ 40% of the total voltage is dropped across the active layer.

In summary therefore the devices reported here have introduced two new elements into high-field EL technology:

(1) A high-efficiency electron injector capable of delivering a macroscopically uniform, high current density at relatively low voltage, with screening against breakdown initiated at the semiconductor-insulator interface.

(2) The possibility of improvements in EL efficiency arising from hot electron injection at the SiO_2 -ZnS heterojunction. However improvements in phosphor material technology may be required before this effect can be realized in practice.

To date useful luminance (78 fL at $\sim 4 \times 10^{-2} \text{ A cm}^{-2}$, 48V) has been achieved without systematic optimization of the structure. These devices operate at lower voltage than typical ACTFEL or powder DCEL cells, and are compatible with conventional Si driving circuitry. The fact that the device is fabricated on a Si substrate also offers the possibility of partial integration of the driving circuits on the active area. The use of single crystal Si substrates would limit display size, but the (Si-rich SiO_2)- SiO_2 electron injector is itself amorphous and therefore suitable for use on larger-area amorphous-Si substrates. The ZnS:Mn light emission is reproducible and uniform, and the B-V characteristic is sufficiently steep to be useful for matrix addressing. A range of colors should be possible using other phosphor layers. The limitation of the devices at the present time appears to be charge trapping in the SiO_2 layer under DC operation, which causes a shift in the I-V characteristic and leads to failure after a few hours operation.

Acknowledgements

The authors are grateful to Dr. P. Alt for assistance in making the luminance measurements.

References

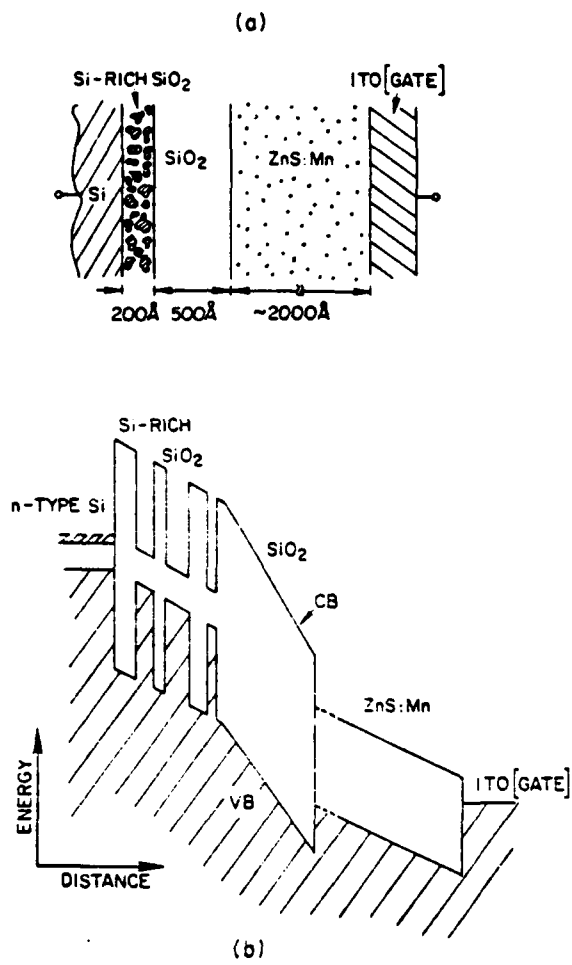
- * Sponsored in part by Defense Advanced Research Projects Agency (DoD) ARPA
Order No. 4012 Under Contract No. MDA903-81-C-0100 issued by Department of
Army, Defense Supply Service-Washington, Washington DC 20310.
- a. On leave from: Royal Signals and Radar Establishment, Malvern, England.
- b. Sponsored in part by Consejo Nacional de Ciencia y Technologia (CONACyT) and
Centro de Investigaciones y Estudios Avanzados del I.P.N. (CIEA), Mexico.
- 1. "Electroluminescence", Topics in Appl. Physics 17, ed. J.I. Pankove, (Springer-Verlag,
Berlin, 1977).
- 2. W. E. Howard, Proc. S.I.D., 22, 47 (1981).
- 3. T. Inoguchi, M. Takeda, Y. Kakihara, Y. Nakata and M. Yoshida, S.I.D. 74 Digest, 84
(1974).
- 4. A. Vecht, N. J. Werring, R. Ellis and P. J. F. Smith, J. Phys. D 2, 953 (1969).
- 5. J. W. Allen, J. Lumin. 7, 228 (1973).
- 6. M. I. Abdalla, J. Thomas, A. Brenac and J-P. Noblanc, IEEE Trans. Electron Dev.
ED-28, 694 (1981).
- 7. H. Ohnishi and Y. Hamakawa, Jap. J. Appl. Phys. 17, 1225 (1978).
- 8. T. Mishima, W. Quan-kun and K. Takahashi, J. Appl. Phys. 52, 5797 (1981).
- 9. J. J. Hanak, Proc. 6th Int. Vac. Congress: Jap. J. Appl. Phys. Suppl. 2, 809 (1974).
- 10. D. J. DiMaria, in "The Physics of MOS Insulators", Proc. of Int. Topical Conference,
ed. G. Lucovsky, S. T. Pantelides and F. L. Galeener, (Pergamon Press, N.Y. 1980),
p. 1.
- 11. D. Dong, E. A. Irene and D. R. Young, J. Electrochem. Soc. 125, 819 (1978).
- 12. D. J. Robbins, C. Falcony, and D. J. DiMaria, unpublished.
- 13. D. J. DiMaria, R. Ghez and D. V. Dong, J. Appl. Phys. 51, 4839 (1980).

14. J. A. Cape, R. D. Ketchpel and L. G. Hale, IEEE Trans. Electron Dev. ED-25, 1352 (1978).
15. D. C. Morton and F. Williams, S.I.D. 81 Digest, 30 (1981).
16. T. Doi, H. Ohnishi and K. Ieyasu, J. Appl. Phys. 51, 4555 (1980).
17. N. T. Gordon, M. D. Ryall and J. W. Allen, Appl. Phys. Lett. 35, 691 (1979).

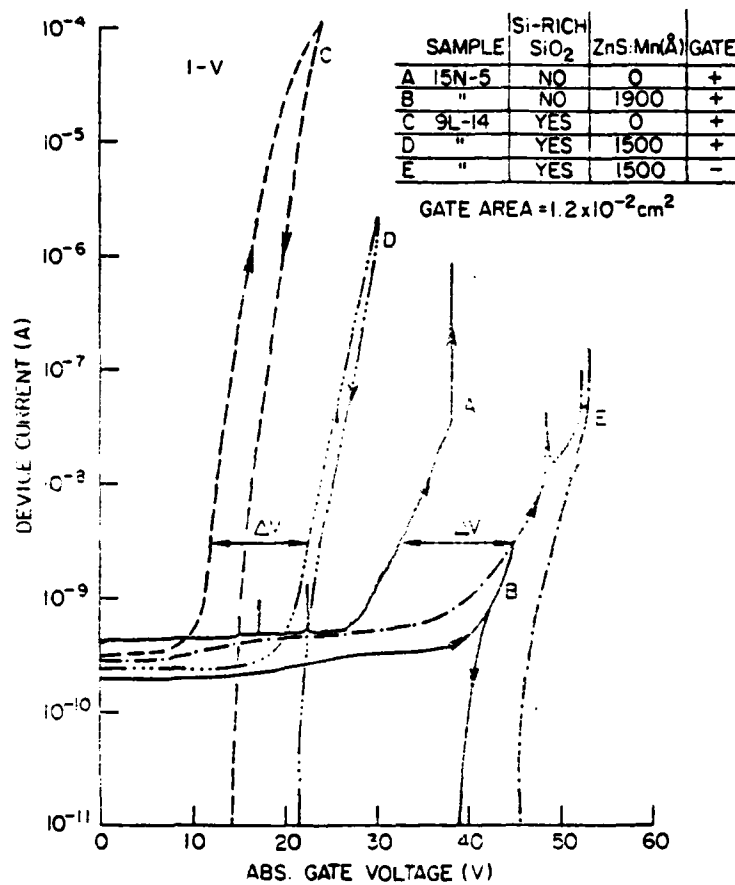
Table 1

External luminous efficiency under d.c. bias (9L-14; electrode area $1.2 \times 10^{-2} \text{cm}^2$)

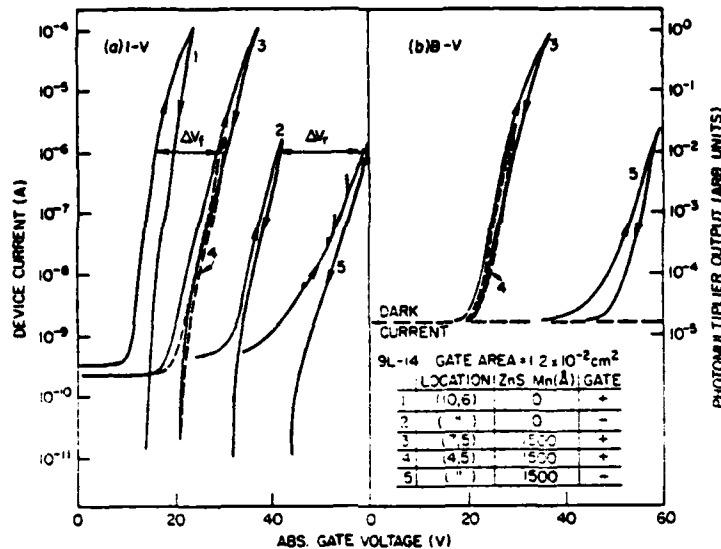
Current (A)	Voltage (V)	Luminance (fL)	Luminous efficiency (lumens W ⁻¹)
1×10^{-6}	35.4	1.0	0.37
3×10^{-6}	37.2	3.3	0.38
1×10^{-5}	39.1	9.9	0.33
3×10^{-5}	40.7	22.6	0.24
1×10^{-4}	42.3	45.5	0.14

**Figure 1**

- (a) Section through a typical EL device.
- (b) Schematic energy level diagram under forward (positive gate) bias. The potential wells in the (Si-rich SiO_2) layer represent the small Si islands.

**Figure 2**

Current-voltage characteristics for a wafer with no (Si-rich SiO₂) layer (15N-5; curves A,B) and a wafer with a 200 Å (Si-rich SiO₂) layer (9L-14; curves C,D,E). Areas with no ZnS:Mn layer are control devices on each wafer. ΔV and $\Delta V'$ represent the voltages across the ZnS:Mn layers on each wafer at a current of $3 \times 10^{-9} \text{ A}$. Active device area is defined by the gate electrode ($1.2 \times 10^{-2} \text{ cm}^2$). Gate polarity is indicated in the inset. Arrows indicate directions of increasing and decreasing ramp voltage.

**Figure 3**

(a) Current-voltage characteristics under forward (+ gate) and reverse (- gate) bias for wafer 9L-14. Gate electrode locations and polarity are indicated in the inset.

(b) Light output-voltage curves corresponding to the appropriate I-V curve in (a).

The reverse bias I-V curve 2 in (a) is determined by tunneling at the ITO/SiO₂ interface, with an effective barrier height ~2.8 eV obtained by fitting the Fowler-Nordheim tunneling equation.¹² This effective barrier height is similar to that at the ZnS/SiO₂ interface (~3.0 eV) which determines curve 5. To a good approximation the voltage differences ΔV_f and ΔV_r therefore represent the voltages across the ZnS:Mn layer under forward and reverse bias at a current of 1×10^{-6} A.

**EXPERIMENTAL TEST OF THE QUANTUM MECHANICAL
IMAGE FORCE THEORY ***

A. Hartstein, Z. A. Weinberg and D. J. DiMaria

with the technical assistance of F. L. Pesavento and J. A. Tornello

**IBM - Thomas J. Watson Research Center
Yorktown Heights, New York**

ABSTRACT

Both photon-assisted-tunneling and internal photoemission measurements have been made on the same metal-oxide-semiconductor (MOS) samples. The effective barrier heights between the metal (Al or Au) and the oxide (SiO_2) extracted from the internal photoemission measurements are found to be larger by ~ 0.3 eV than the effective barrier heights extracted from the photon-assisted-tunneling measurements. Only the quantum mechanical image force theory is capable of explaining this result.

*This work was sponsored by Defense Advanced Research Projects Agency (DoD) ARPA Order No. 4012 Under Contract No. MDA903-81-C-0100 issued by Department of Army, Defense Supply Service-Washington, Washington D.C. 20310.

I. INTRODUCTION

Photon-assisted-tunneling measurements have demonstrated that the classical image force theory does not provide the proper description of the interaction between tunneling electrons and the metal from which they emerge.^{1,2} Internal photoemission measurements on the other hand have long been interpreted in terms of the classical image force.^{3,4} A qualitative explanation of these seemingly contradictory results has been given in terms of a quantum-mechanical formulation of the image force problem.⁵ The quantum mechanical image force theory was then shown to be qualitatively consistent with both photon-assisted-tunneling and internal photoemission measurements.⁶ The purpose of this study was to test the quantitative fit of the quantum mechanical image force theory with both the photon-assisted-tunneling experiments and the internal photoemission experiments by doing accurate measurements on the same samples. In particular we wanted to explore the theoretical prediction⁶ that the effective barrier heights between the metal and insulator derived from the two experiments would differ by about 0.2 eV.

The physical situation which we are considering for both the experiments and the theoretical calculations is illustrated in Fig. 1. The conduction band edge (E_c) in the insulator (SiO_2) and the Fermi energy (E_F) in the metal (Al or Au) are shown. The triangular shape for the potential is the result of an applied electric field F . The image force potential is not shown. Photon-

assisted-tunneling involves the photoexcitation of an electron by an energy, $h\nu_1$, less than the barrier height and the subsequent tunneling of the electron through the barrier. Internal photoemission involves the photoexcitation of an electron by an energy, $h\nu_2$, greater than the barrier height and the subsequent transmission of the electron over the barrier. The current measured in a particular experiment is the sum of the contributions from all of the electrons incident on the barrier. From this brief introduction it is clear why a single unified theory is necessary for the description of both processes.

In this paper we report the experimental study of both the photon-assisted-tunneling and the internal photoemission at the Al/SiO₂ and the Au/SiO₂ interfaces. These experiments are described in detail in Section II. The main result is that the effective barrier heights extracted from the internal photoemission measurements are ~0.3 eV larger than the effective barrier heights extracted from the photon-assisted-tunneling measurements. This is in agreement with the quantum mechanical image force theory. In Section III both the classical and quantum mechanical image force theories are reviewed, and some new numerical results are presented. In Section IV the theories are compared to experiment and the results are discussed. It is found that the quantum mechanical image force theory gives the best description of the experimental results. However, the theory in its present form is not capable of complete quantitative agreement with all aspects of the experimental observations.

II. EXPERIMENT

The samples used in this study were MOS capacitors formed on (100) oriented 1 Ω-cm p-type silicon wafers. Oxides were thermally grown at 1000 C in a dry oxygen ambient and annealed in nitrogen. The oxide thicknesses were 301 Å for the Al sample and 209 Å for the Au sample. These thicknesses were chosen to minimize the effects of optical interference in the MOS structure and at the same time to minimize the dark currents in the devices. The capacitors were formed by evaporating 0.5 mm metal dots on the oxides. The semitransparent Al dots were 135 Å thick, and the semitransparent Au dots were 200 Å thick.

We studied two wafers with Al counter electrodes and one wafer with Au counter electrodes. Several samples were studied on each wafer, and measurements were made on samples prepared both with and without post-metal anneals. Quantitative differences in the measurements were seen for the different sample treatments. The effect of post-metal anneal on internal photoemission measurements has already been studied.⁷ A less detailed account of the effects of sample preparation on photon-assisted-tunneling measurements has also been given.² In this paper we seek to test the various theories of photon-assisted-tunneling and internal photoemission. Therefore, we made all of our measurements on one sample, and then repeated the procedure several times. Variations from sample to sample were observed in

the barrier heights and dielectric constant, but the general trends discussed below were the same for all samples.

The physical arrangement for the experiments is shown schematically in Fig. 2. Monochromatic light is incident on the MOS sample from either a laser or a monochromator. The current is then measured as a function of applied voltage both with light on and off. The difference between these two values is the photocurrent. The photoyield is then determined by normalizing the current to the number of photons absorbed in the metal gate. This involves correcting for the source intensity (laser or monochromator), the absorption spectrum of the metal, the photon energy and the interference of the incident light in the MOS structure. All of the data were normalized in this manner.

The photon-assisted-tunneling measurements were performed using an argon laser. The experimental technique has been discussed in some detail previously.^{1,2} A prism was used to disperse the laser light to filter out any unwanted wavelengths present in the laser beam. For the case of the Al samples four wavelengths in the visible were used. They were 514.5 nm, 488.0 nm, 476.5 nm and 457.9 nm. For the Au samples two ultraviolet wavelengths of the argon laser were used. They were 363.8 nm and 351.1 nm.

The data for one of the Al samples is shown in Fig. 3 and the data for Au is shown in Fig. 4. The data is plotted on a standard Fowler-Nordheim

tunneling plot. The wavelengths of the incident light for each curve is indicated in the figures. The solid curves represent a one parameter fit for each set of data. The theory used was the Fowler-Nordheim tunneling theory which neglects image force.¹ For the range of photon energies used, that theory is equivalent to the quantum mechanical image force theory because the quantum mechanical image force becomes negligibly small in the tunneling regime. The parameter in the fit is the barrier height between the appropriate metal and the SiO₂ conduction band edge. For the Al sample shown the barrier was $\phi = 3.25 \pm .01$ eV, and for the Au sample the barrier height was $\phi = 3.91 \pm .01$ eV.

The deviations of the data from the theory at high electric fields are observed for non-post metal annealed samples but not for the annealed samples used previously.¹ However, the internal photoemission measurements which will be discussed below give better results on unannealed samples.⁷ Therefore, we chose to use the samples, unannealed, which would yield the best results on the most difficult part of our experiments, namely the internal photoemission measurements. Whatever uncertainties arise in the barrier determinations from these photon-assisted-tunneling measurements, they are small compared to the uncertainties in the barriers measured by internal photoemission as discussed below. Our choice of samples then minimizes the overall uncertainties in the experiments.

The internal photoemission measurements were performed using a monochromator system described elsewhere.⁷ The data obtained for an Al sample are shown in Fig. 5. The data obtained for a Au sample are shown in Fig. 6. These are standard plots for internal photoemission measurements and show the same qualitative features which have been seen many times before. The parameters on the curves are the applied voltages for each curve. Only a portion of the data is displayed so as not to crowd the figures.

We analysed these data in the conventional way utilizing the classical image force theory. That theory gives⁴

$$I(h\nu, F) \propto (h\nu - \phi_B + KF^{1/2})^2, \quad (1)$$

where I is the photocurrent, $h\nu$ is the photon energy, F is the applied electric field, ϕ_B is the interface barrier energy, and K is a constant. The experimentally determined electric field F is given by $F = (V - \phi_{ms})/d_{ox}$, where V is the applied voltage, ϕ_{ms} is the contact potential difference between the appropriate metal and the Si substrate, and d_{ox} is the oxide thickness.

Using this theory, we extrapolated the straight line portion of the curves in Figs. 5 and 6 to zero yield and determined the barriers, $\phi(F) = \phi_B - KF^{1/2}$. This extrapolation is clearly an important step in the data analysis. Since all of the theories predict a linear range at high photon energy and a tail at low energy, we extrapolated only the linear portion of the data at high photon energies as shown in the figures. The numerical results of the theories were

also extrapolated in the same way. We then plotted these barriers as a function of $F^{1/2}$. The extrapolations of these lines to zero field give the barrier heights derived from the internal photoemission measurements. Fig. 7 shows these curves for the Al and Au samples. The barrier height determined in this way for the Al sample is $\phi_B = 3.6$ eV, and for the Au sample the barrier height is $\phi_B = 4.2$ eV. The average difference between these barriers determined from internal photoemission measurements and the corresponding barriers determined from photon-assisted-tunneling measurements was found to be ~ 0.3 eV.

It must be emphasized that the barrier heights determined in this manner from the internal photoemission measurements are very sensitive to which portion of the data is fit linearly. For example, if more of the lower energy points were included in the fit for the Al data in Fig. 5, a barrier height as low as ~ 3.2 eV could be extracted. This is what has usually been done by other researchers in the past.⁷ In order to accurately compare theory and experiment, we have extrapolated the more easily recognized linear portions of both the experimental and theoretical curves rather than making an arbitrary extrapolation, which includes the curved portions of the data, as has been done in the past. For this reason, our quoted values of the barrier heights derived from internal photoemission are somewhat higher than values found in the literature.

The slopes of the curves in Fig. 7 are the constant K in the classical theory. The slope is related to the dielectric constant of the insulator by the expression $K = (e^3/4\pi\epsilon_0\epsilon)^{1/2}$, where ϵ_0 is the dielectric permittivity of free space, and $\epsilon = 2.15$, the optical dielectric constant of SiO_2 . From the data shown we find values of $\epsilon = 2.3$ for the Al/SiO_2 interface and $\epsilon = 3.1$ for the Au/SiO_2 interface. Even wider variations in the values of ϵ have been reported when different processing conditions have been studied.⁷ We will have more to say on this subject in the later sections, but the determination of ϵ both experimentally and theoretically is the weakest part of our results, and quantitative comparisons are difficult at best.

III. THEORY

The arguments which lead to the formulation of the quantum mechanical image force potential have been given in Ref. 5. The calculation which gives the numerical results that can be compared to the internal photoemission and photon-assisted-tunneling measurements has been given in Ref. 6. In this section we review that theory and present the results which pertain to the present experiments.

We consider the problem of an electron in a metal which is incident on the interface with an insulator. What we ultimately want to calculate is the transmission probability of the electron through the interface. The wave function of the electron is denoted by $\psi(x,t)$. We want to describe the inter-

action between this electron and the remaining electrons in the metal as the electron attempts to tunnel into the insulator. Since all of the electrons move on the same time scale, a Hartree-Fock type description is adopted. Therefore, the wave function of the incident electron must be adjusted self-consistently to the wave function of the plasma. The wave function of the plasma in this approximation becomes an image of that portion of the wave function of the incident electron which is in the insulator. The image force potential is then derived from the force on a test charge in the insulator and is given by⁵

$$V_{IM} = - \int_0^{\infty} \left[\frac{e^2 |\psi(x',t)|^2}{8\pi\epsilon_0\epsilon(x+x')} \right] dx', \quad (2)$$

where ϵ_0 is the dielectric permittivity of free space, ϵ is the dielectric constant of the insulator, and x is the distance of the test charge from the interface. A similar result has been derived rigorously for the case where the image force arises from the interaction of an external electron with the surface optical phonons of a dielectric medium.⁶

This potential must now be inserted into the Schrödinger equation in order to calculate the transmission of the interface. This is a very difficult problem, hence we make an important simplifying assumption. We approximate the square of the wave function of the incident electron as a δ function, $|\psi(x,t)|^2 = \delta(x'-x,t)$. After the electron interacts with the barrier, the square of the wave function in the insulator will be $T\delta(x'-x,t)$, where T is the self-consistent

transmission of the barrier. This approximation is good as long as the portion of the electron wave function in the insulator remains well localized after it interacts with the barrier. The image force potential is then given by

$$V_{IM} = -Te^2/16\pi\epsilon_0\epsilon x , \quad (3)$$

i.e., it is the classical result scaled by the transmission of the barrier. For energies far above the top of the barrier, where the electron can be assumed to be a point charge, $T \approx 1$ and Eq. (3) reduces to the classical result. Far below the top of the barrier $T \approx 0$, and the image force is negligibly small. Equation (3) is thus an approximation for the important region near the top of the barrier.

The complete potential which an electron sees in the barrier region is then given by

$$V = \phi_B - eFx - Te^2/16\pi\epsilon_0\epsilon x , \quad (4)$$

where the first term gives the energy difference between the conduction band edge of the insulator and the Fermi level of the metal, the second term is the potential in the applied electric field, and the last term is the image force potential. The transmission of the interface is then calculated by a numerical integration of the Schrödinger equation across the interface, iterating until a self-consistent solution is obtained.

In Fig. 8 we show the transmission probability of an Al/SiO₂ interface for an applied electric field of 5×10^6 V/cm. The figure shows the transmission probability as a function of electron energy. The three curves shown are calculated for the classical image force, the quantum mechanical image force, and for no image force. In each case the transmission probability changes abruptly near the barrier height (3.25 eV). It is clear that the results of the quantum mechanical image force model approach the results of the classical image force model for large energy, and approach the results of the no image force calculation for small electron energy.

The current measured in an experiment is obtained by summing the transmission probabilities for the incident electrons over the supply function in the metal. The supply function gives the number of electrons incident on the barrier with a particular perpendicular component of momentum. The expression for the current becomes⁹

$$I(h\nu, F) = A \int_{-\infty}^{\infty} S(E, h\nu) T(F, E) dE , \quad (5)$$

where A is the equilibrium number of photoexcited electrons, $S(E, h\nu) = \ln[1 + \exp(E_F + h\nu - E)/kT]$ is the supply function for electrons, T(F, E) is the barrier transmission probability, $h\nu$ is the photon energy, and E_F is the Fermi energy in the metal. In the classical limit, T=1 above the barrier, Eq. 5 reduces to Eq. 1.

This theory⁶ has been used to calculate the photoyield for both photon-assisted-tunneling and internal photoemission experiments at the Al/SiO₂ interface. In this paper we extend this calculation to the Au/SiO₂ interface. Qualitatively the results are the same. In the photon-assisted-tunneling regime this theory gives the same results as a no image force theory¹ because the quantum mechanical image force potential is negligibly small.

The results of the internal photoemission calculation for the Al/SiO₂ interface are shown in Fig. 9. The calculations for the Au/SiO₂ interface show the same qualitative features. These curves were analysed, to obtain the effective barrier heights and the effective dielectric permittivities, by the procedure outlined in the experimental section. In each case the effective barrier height, obtained from the internal photoemission curves, was found to be ~0.2 eV larger than the assumed barrier height in the calculation. The barrier heights obtained from the photon-assisted-tunneling curves were the same as the values used in the calculations. Thus the theory predicts that the analysis of the two experiments should yield different barrier heights as was found experimentally in Section II.

The effective dielectric permittivity, derived from the slope of the theoretically calculated barrier heights vs. $F^{1/2}$ curves, is found to depend on the metal parameters. The theoretical value $\epsilon = 2.05$ reported earlier⁶ is incorrect due to a numerical error in the calculation, and should have been a factor of 4

larger, $\epsilon = 8.2$. The present results will be discussed in more detail in the next section.

IV. RESULTS AND DISCUSSION

In order for the calculations to be compared to the experimental results in more than a qualitative way, it was necessary to choose appropriate parameters for the calculations. The parameters which were chosen to characterize the SiO_2 were an effective mass,¹⁰ $m^* = 0.5m_e$ and $\epsilon = 2.15$. For the case of Al, the barrier height was chosen to be $\phi_B = 3.25$ eV as determined from the photon-assisted-tunneling measurements, and the Fermi energy was taken to be 11.5 eV¹¹ above the conduction band minimum. For the case of Au, the barrier height was chosen to be $\phi_B = 3.91$ eV, and the Fermi energy was taken to be 5.51 eV.¹² The results of the calculation for the Al/ SiO_2 interface are shown in Fig. 9. The curves for the Au/ SiO_2 interface are very similar, showing a shift in the curves with barrier height.

It is clear that both the experimental and theoretical curves have the same qualitative features. Each has a linear portion of the curves at high photon energies and a tail at low photon energies. This tail is not predicted by the simple classical theory, but it is predicted by a quantum mechanical calculation using the classical image force potential as well as by the full quantum mechanical theory. In order to compare theory and experiment quantitatively, we extrapolated the linear portion of the theoretical curves to field dependent

effective barrier heights, ϕ , as we did for the experimental curves. These barriers were then plotted as a function of $F^{1/2}$ along with the experimental curves derived earlier. The results of this analysis for the Al/SiO₂ interface are shown in Fig. 10, and the results for the Au/SiO₂ interface are shown in Fig. 11.

Each figure shows the experimental data as points compared to three theories. The solid lines are the results of the quantum mechanical image force theory described in Section III. The dashed curves are the results of our quantum mechanical calculation using the classical image force potential. This used the same computer program as the full quantum mechanical theory, but with the classical image force potential. The dot-dashed curves are the results of the simple classical image force theory. It is clear that the data show a better fit to the quantum mechanical image force theory than to either of the other theories. However, it is also clear that the quantum mechanical image force theory does not accurately predict the slopes of these curves.

In these figures both the simple classical image force model and the quantum mechanical calculation of the classical image force potential show barriers which extrapolate approximately to the barrier assumed in the calculation, i.e., the barrier derived from the photon-assisted-tunneling measurements. The curves and data shown in the figures were extrapolated using a simple linear least squared fit. Neither the experiments nor the quantum mechanical image force theory show the same barrier heights. In this respect

the quantum mechanical theory is qualitatively different and better fits the experimental results.

It is extremely difficult to assess the degree to which the theories adequately predict the slopes of these curves. For the Au/SiO₂ interface the fit to the quantum mechanical image force theory is not too bad, but for the Al/SiO₂ interface the fit is not as good. To make matters worse there are large uncertainties in the slopes as derived from the experiments. Qualitatively, both quantum mechanical calculations show slopes which depend on material parameters as seems to be the case from the experiments. The simple classical model does not show this dependence.

In Fig. 12 we show a direct comparison between the quantum mechanical image force theory and the internal photoemission measurements for both Al and Au. The figure only shows data for $F = 3 \times 10^6$ V/cm, where the derived curves of Figs. 10 and 11 fit reasonably well. As can be seen, the theory fits very well for the Au/SiO₂ interface and somewhat less well for the Al/SiO₂ interface. The main purpose in showing these curves is to show a direct comparison between theory and experiment with a minimum of data analysis in between. The agreement between theory and experiment shown is as good as can be expected from a theory which does not adequately predict the field dependence of internal photoemission. In fact none of the theories adequately predicts the observed field dependences.

On the whole the quantum mechanical image force theory, presented in Section III, does the best overall job of predicting the experimental results. It is the only theory which predicts that the barrier heights derived from the internal photoemission measurements should be larger than the barrier heights derived from the photon-assisted-tunneling measurements. It is also the only theory which includes an image force and can fit the form of the photon-assisted-tunneling experiments accurately.¹ It does, however, have the drawback that it does not give a complete quantitative description of the experiments. Perhaps this comes from the approximations used in arriving at a tractable theory from which to perform numerical calculations. It is quite conceivable that a more accurate calculation based on these ideas will give a better quantitative fit.

V. CONCLUSIONS

We have measured both photon-assisted-tunneling and internal photoemission curves on the same MOS samples. We find that the effective barrier heights extracted from the internal photoemission experiments, by extrapolating the linear portion of the curves, are larger than the effective barrier heights extracted from the photon-assisted-tunneling experiments by about ~0.3 eV. Only the quantum mechanical image force theory is capable of explaining this result.

VI. ACKNOWLEDGEMENTS

The authors would like to acknowledge J. A. Tornello for help with the sample preparation, and S. K. Lai and F. L. Pesavento for help with the internal photoemission measurements. We would also like to thank P. M. Solomon for many helpful discussions.

REFERENCES

1. Z. A. Weinberg and A. Hartstein, Solid State Commun. **20**, 179 (1976).
2. A. Hartstein, Z. A. Weinberg, and D. J. DiMaria, *Physics of SiO₂ and its Interfaces*, edited by S. T. Pantelides (Pergamon, New York, 1978), p. 51.
3. B. E. Deal, E. H. Snow, and C. A. Mead, J. Phys. Chem. Solids **27**, 1873 (1966).
4. R. J. Powell, J. Appl. Phys. **41**, 2424 (1970).
5. A. Hartstein and Z. A. Weinberg, J. Phys. C **11**, L469 (1978).
6. A. Hartstein and Z. A. Weinberg, Phys. Rev. B **20**, 1335 (1979).
7. P. M. Solomon and D. J. DiMaria, J. Appl. Phys. **52**, 5867 (1981).
8. E. Evans and D. L. Mills, Phys. Rev. B **8**, 4004 (1973).
9. E. L. Murphy and R. H. Good, Phys. Rev. **102**, 1464 (1956).
10. A critical review of the literature reveals that this is the most appropriate value for m*, Z. A. Weinberg, to be published.
11. B. Segall, Phys. Rev. **124**, 1797 (1961).
12. C. Kittel, *Intro. to Solid State Physics, 2nd Edition*, (John Wiley & Sons, New York, 1956), p. 250.

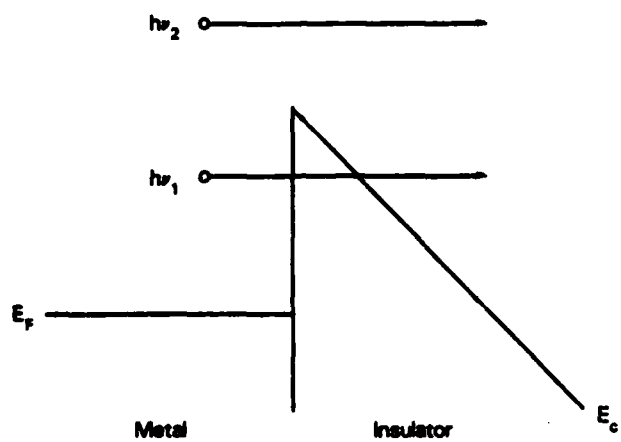


Fig. 1 - The electronic structure of the interface illustrating electrons both tunneling through the interfacial barrier ($h\nu_1$) and passing over the barrier ($h\nu_2$) following photoexcitation. E_F is the Fermi energy in the metal, and E_c is the conduction band edge in the insulator.

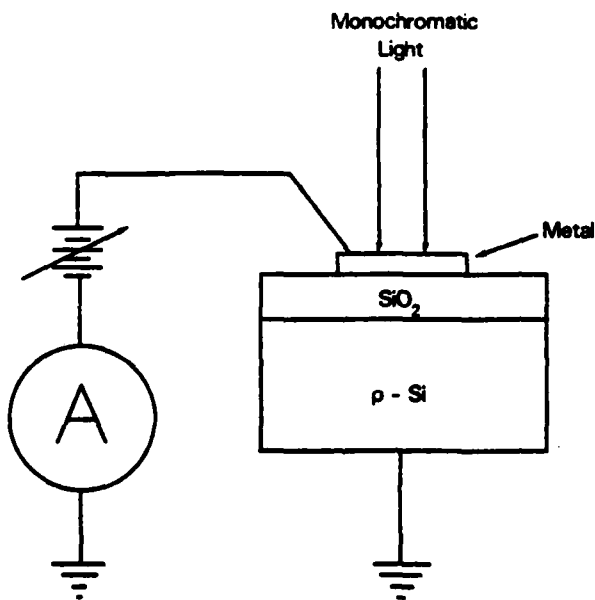


Fig. 2 - Schematic representation of the experimental arrangement. Monochromatic light is incident on the MOS sample. The resulting photocurrent is measured using a sensitive picoammeter.

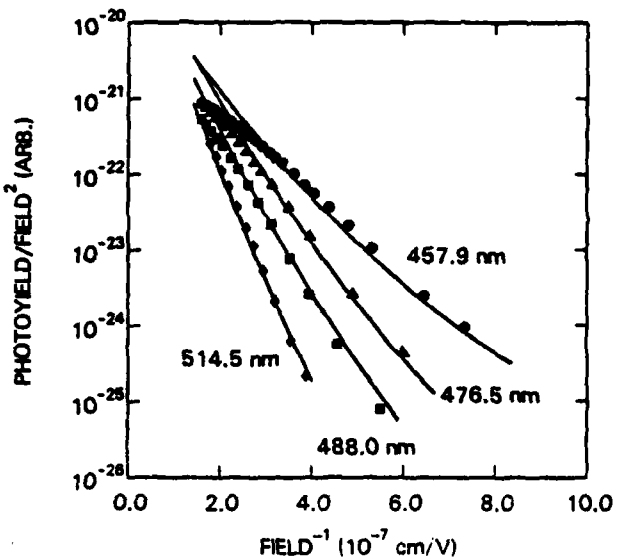


Fig. 3 - Photon-assisted-tunneling characteristics of the Al/SiO₂ interface.

Each curve is for a different laser wavelength. The solid curves are the theory and the points are the experimental data.

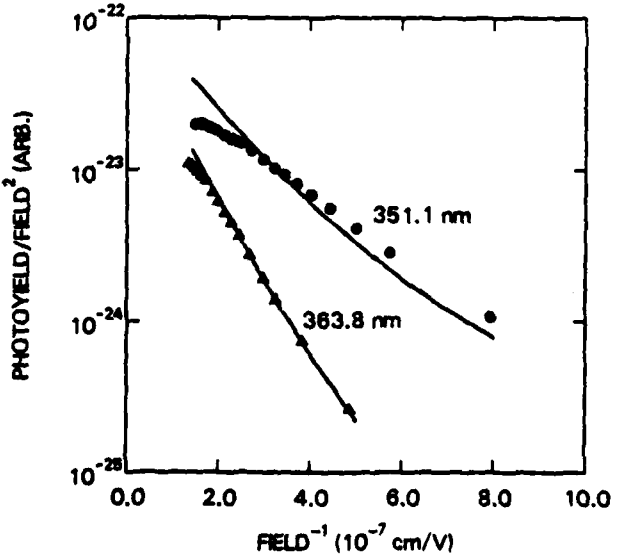


Fig. 4 - Photon-assisted-tunneling characteristics of the Au/SiO₂ interface.

Two laser wavelengths are shown. The solid lines are the theory and the points are the experimental data.

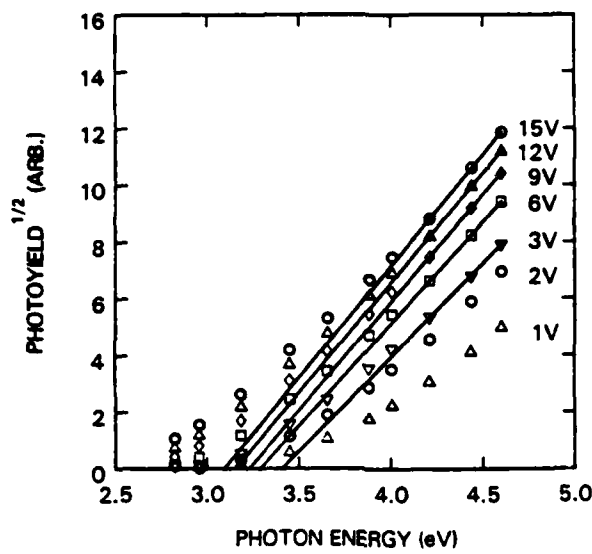


Fig. 5 - Internal photoemission characteristics for an Al/SiO₂ interface. The points are experimental data and the solid lines are the extrapolations made to zero photoyield. Each curve is labelled by the voltage applied to the device. Extrapolations were not made for the lowest voltages where the errors in extrapolation would be the largest.

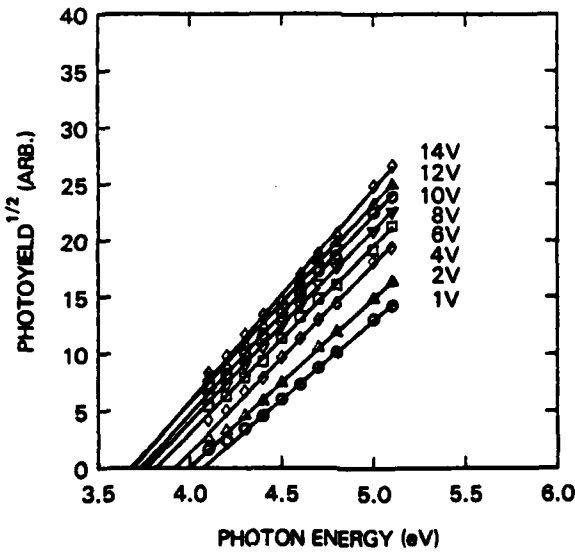


Fig. 6 - Internal photoemission characteristics for a Au/SiO₂ interface. The points are experimental data and the solid lines are the extrapolations made to zero photoyield. Each curve is labelled by the voltage applied to the device.

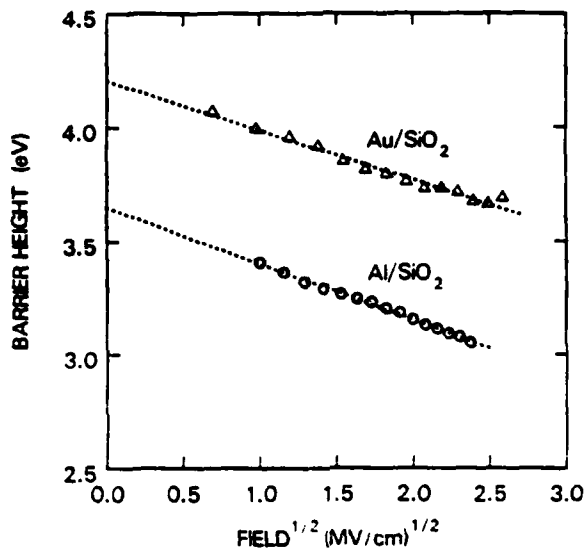


Fig. 7 - Effective barrier heights as a function of applied electric field. The circles are for Al and the triangles are for Au. The dotted lines are linear fits to the data. The extrapolation of the curves to zero field is the effective barrier height of the interface, and the slope of the curves is related to the dielectric constant of the insulator.

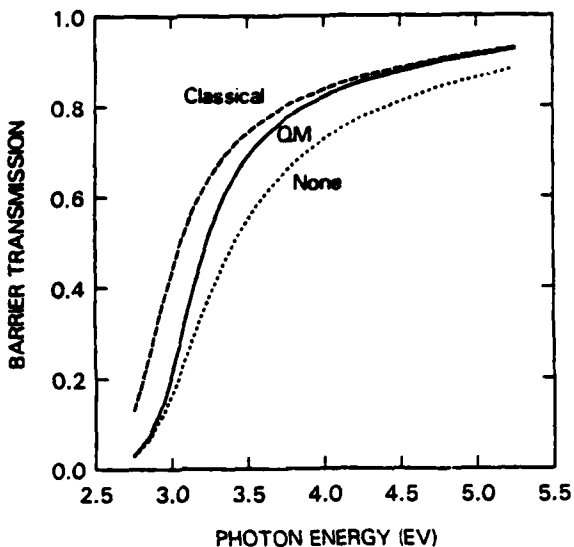


Fig. 8 - Barrier transmission probability for an Al/SiO₂ interface calculated for an applied electric field of 5×10^6 V/cm. The barrier occurs at an energy of 3.25 eV. The solid curve is for the quantum mechanical image force potential; the dashed curve is for the classical image force potential; and the dotted curve is for the potential with no image force included.

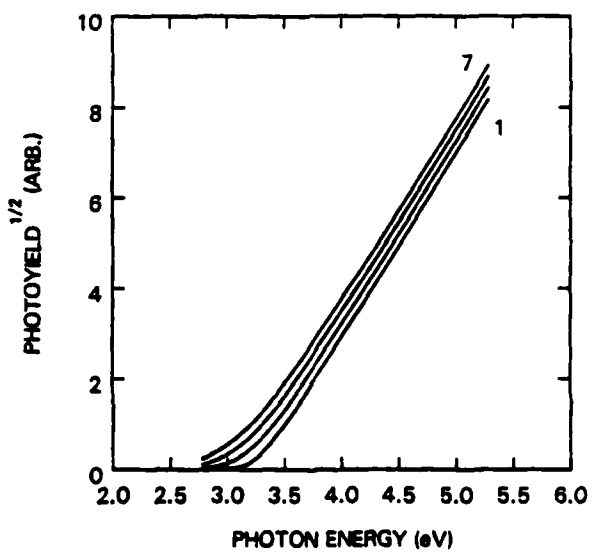


Fig. 9 - Theoretical internal photoemission curves calculated using the quantum mechanical image force theory for the Al/SiO₂ interface. The curves shown are for $(1.3, 5.7) \times 10^6$ V/cm applied electric field.

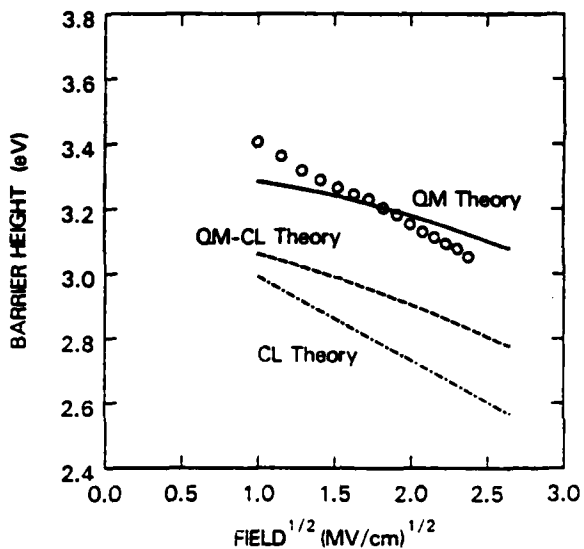


Fig. 10 - Comparison of the experimental and theoretical effective barrier heights as a function of electric field for the Al/SiO₂ interface. The solid curve is for the quantum mechanical image force theory (QM); the dashed curve is for a quantum mechanical calculation of the classical image force (QM-CL); and the dot-dashed curve is the simple classical model (CL).

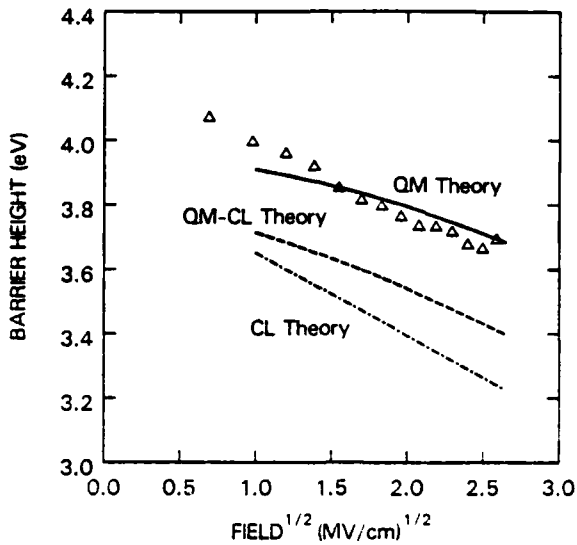


Fig. 11 - Comparison of the experimental and theoretical effective barrier heights as a function of electric field for the Au/SiO₂ interface. The solid curve is for the quantum mechanical image force theory (QM); the dashed curve is for a quantum mechanical calculation of the classical image force (QM-CL); and the dot-dashed curve is the simple classical model (CL).

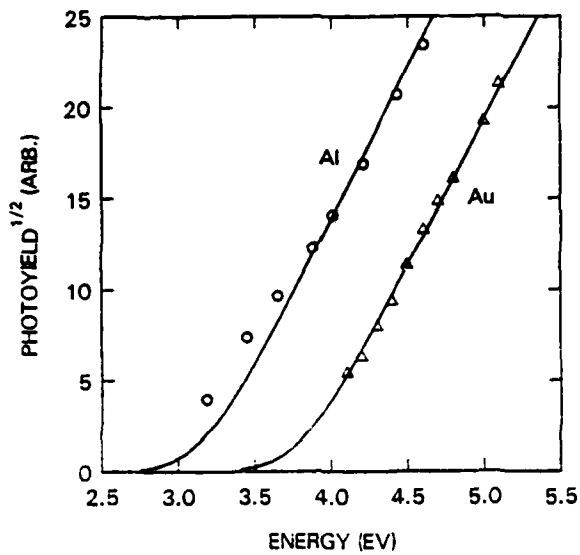


Fig. 12 - Direct comparison between the quantum mechanical image force theory and the internal photoemission measurements. The curves are shown for an applied field of $F = 3 \times 10^6$ V/cm. The circles are data for Au and the triangles are data for Al. The solid lines are the theoretical curves.

Evidence for a parallel path oxidation mechanism at the Si-SiO₂ interface

E. A. Irene

IBM Thomas J. Watson Research Center, Yorktown Heights, New York 10592

(Received 13 August 1981; accepted for publication 22 October 1981)

Some controversy exists as to whether the reaction of oxygen and Si at the Si-SiO₂ interface involves both atomic and molecular oxygen. From the direction of curvature of Arrhenius plots for the observed rate constants substantial support is obtained for the mechanism with two oxidant species. The direction of curvature was obtained from the second derivative of $\ln k_{\text{obs}}$ with respect to T^{-1} . Parallel rate processes yield concave upwards Arrhenius plots while consecutive processes yield concave downwards plots.

PACS numbers: 82.65.Nz, 81.60.Dq, 82.20.Pm

The mechanism for the oxidation of single crystal silicon is phenomenologically characterized by linear parabolic kinetics for SiO₂ film thicker than L_0 according to the relationship¹

$$t - t_0 = k_L^{-1}(L - L_0) + k_p^{-1}(L^2 - L_0^2), \quad (1)$$

where t is the time for oxidation, L is the oxide thickness, k_L and k_p are the linear and parabolic rate constants, respectively. L_0 and t_0 represent the lower limit of the linear parabolic regime. The linear part of this oxidation model arises from interface kinetics, while the parabolic behavior, which predominates at large L , occurs because of transport of oxidant across the oxide film. For the linear interfacial kinetics, Ghez and van der Meulen² proposed an atomistic reaction mechanism involving the reaction both atomic and molecular oxygen with Si at the Si-SiO₂ interface. This proposition was deduced from experimental pressure dependencies of k_L and predictions from the two oxidant species mechanism. Later Blanc³ proposed a similar mechanism to explain the early rapid oxidation regime except that Blanc argued that the reaction of oxygen atoms predominates. Totally independent of this work, Irene and Dong⁴ reported curved Arrhenius plots ($\ln k_L$ vs $1/T$) using k_L values computed from extensive oxidation data obtained over a wide temperature range (780–1100 °C). The present study will demonstrate that the direction of the curvature of the Arrhenius plots of k_L values i.e., concave upwards, is consistent with the parallel paths mechanism proposed by Ghez and van der Meulen, thereby supporting the oxidation of silicon by both oxygen atoms and molecules.

Consider the parallel paths at the Si-SiO₂ interface to be



and



where the atomic oxygen arises from the equilibrium



The overall rate of formation of SiO₂ is simply the sum of the contributions from (2) and (3) above and the observed composite rate constant is given as

$$k_{\text{obs}} = k_1 + k_2 = k_L. \quad (5)$$

The first derivative of $\ln k_{\text{obs}}$ with respect to T^{-1} yields the Arrhenius plot. For a kinetically simple process, the plot will be linear with a slope proportional to the activation energy for the process. For a nonsimple process, k_{obs} is a composite rate constant and the Arrhenius plot will show curvature. Specifically for the parallel path process given by Eq. (5), the first derivative is

$$\frac{d(\ln k_{\text{obs}})}{d(1/T)} = -\frac{1}{R} \left(E_1 - \frac{k_2/k_1(E_2 - E_1)}{1 + k_2/k_1} \right), \quad (6)$$

under the assumptions that each rate step obeys the Arrhenius equation of the form

$$k = k_0 e^{-E/RT} \quad (7)$$

and k_0 and E are not functions of T . The second derivative is needed to test for the direction of curvature and is given by

$$\frac{d(\ln k_{\text{obs}})^2}{d^2(1/T)} = \frac{1}{R} \left(\frac{(E_2 - E_1)^2 k_2/k_1}{(1 + k_2/k_1)^2} \right). \quad (8)$$

The second derivative test for concavity of functions shows that a positive second derivative is indicative of a curve that

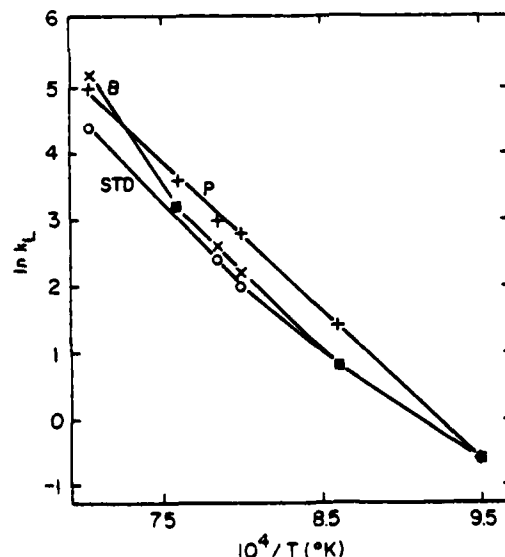


FIG. 1. Arrhenius plot for the linear rate constant k_L for Si oxidation in dry oxygen over the temperature range 780–1100 °C from Ref. 4. It is seen that the lightly doped, STD, and B-doped samples are concave upwards.

is concave upwards (see for example Ref. 5). Equation (8) is everywhere positive hence, the Arrhenius plot for k_{obs} should be concave upwards. Experimental data from Ref. 4 is shown in Fig. 1. It is seen that the Arrhenius plot for k_L which is k_{obs} for the interface reaction is concave upwards, thereby supporting the parallel path mechanism proposed by Ghez and van der Meulen.² The curvature of the Arrhenius plot indicates that k_{obs} is a composite rate constant and therefore not governed by a dominant activation energy.

It is easily shown that for the rates constants of the form of Eq. (7) for any k_{obs} of the form

$$k_{obs} = \sum k_i \quad (9)$$

the second derivative is positive. Similarly, for consecutive rate processes which can be characterized as series conductances by

$$1/k_{obs} = \sum 1/k_i, \quad (10)$$

and where Eq. (7) holds, the second derivative can be shown to be always negative. A negative second derivative indicates an Arrhenius plot that is concave downwards.

Firstly, it was shown that the dual oxidant species

mechanism for the interface reaction of Si and oxidant as proposed by Ghez and van der Meulen not only yields the required pressure dependence² but yields the correct shape for the Arrhenius plot. Secondly, it was shown that it is possible to make deductions concerning the fundamental nature of rate processes from a knowledge of the curvature of Arrhenius plots.

The author is grateful to Dr. R. Ghez for helpful discussions. This work was partially sponsored by Defence Advanced Research Projects Agency (DOD), ARPA Order No. 4012, Under Contract No. MDA903-81-C-0100 issued by Department of Army, Defense Supply Service-Washington, Washington, DC 20310.

¹B. E. Deal and A. S. Grove, *J. Appl. Phys.* **36**, 3770 (1965).

²R. Ghez and Y. J. van der Meulen, *J. Electrochem. Soc.* **119**, 1100 (1972).

³J. Blanc, *Appl. Phys. Lett.* **33**, 424 (1978).

⁴E. A. Irene and D. W. Dong, *J. Electrochem. Soc.* **125**, 1146 (1978).

⁵R. E. Johnson and F. L. Kiokemeister, *Calculus with Analytic Geometry*

(Allyn and Bacon, Boston, 1959) p. 128.

Silicon Oxidation Studies: Measurement of the Diffusion of Oxidant in SiO_2 Films **

E. A. Irene*

IBM Thomas J. Watson Research Center, Yorktown Heights, New York 10598

ABSTRACT

A method for the measurement of the diffusion of oxidant through a growing SiO_2 film is presented. The procedure is based on so-called lag-time diffusion methods in which the time to achieve steady-state oxidation is measured using *in situ* ellipsometry. Two different modes of oxidant transport were observed over the range of temperatures investigated (600° - 1000°C). At temperatures of 900°C and below, no lag-time was observed, and steady-state oxidation was seen at the outset of oxidation. At 1000°C , a lag-time was measured which yielded a value for the diffusion constant, $D = 2.3 \times 10^{-13} \text{ cm}^2/\text{sec}$ for dry O_2 , and this value increased to $2.4 \times 10^{-12} \text{ cm}^2/\text{sec}$ for 1000 ppm H_2 in O_2 . This study provides clear evidence for different dominant modes of oxidation at higher and lower oxidation temperatures.

The thermal oxidation of silicon is generally believed to proceed by a process that encompasses a steady state of both diffusion of oxidant through an SiO_2 film and reaction of this oxidant with Si at the Si- SiO_2 interface. This notion of the mechanism of oxidation of silicon is primarily due to the success of the linear-parabolic oxidation model (1) in correlating the silicon oxidation data [see for example early reports in Ref. (2 and 3)]. Virtually every worker in this field has reported parabolic-like behavior, i.e., a decrease in the thermal oxidation rate of silicon with time. This plus the several studies that show that oxidant rather than silicon is the primary transported species (4-6) support the diffusion-reaction model. The statistical treatment of copious oxidation data demonstrate reasonable predictability (less than 10% error) of this model (7-9). However, this model is largely phenomenological and therefore contributes only little to the understanding of the details of the oxidation mechanism.

The present study is aimed toward a better understanding of the details of the transport of oxidant across the SiO_2 film. To probe this transport process, the well-known lag-time diffusion technique (10, 11) for thin membranes has been adapted to measure the oxidant transport during oxidation. Basically, the oxidation process is followed using *in situ* ellipsometry. The analytical technique assumes Fickian diffusion of oxidant through the growing oxide film, i.e., transport in response to a concentration gradient, and can therefore be used to test for true diffusion as the dominant mode of oxidant transport.

In the literature, there exists diffusion data for oxygen in fused silica (12-15). These studies report divergent values for both the diffusion constant, D , (several orders of magnitude) and the activation energy for diffusion (a factor of more than three). Diffusion data for oxygen in thin films of SiO_2 has to my knowledge not been reported. Since it is known (16) that the precise method of preparation (temperature, impurities, etc.) of amorphous materials determines many of the physical properties of the material, it is likely that part of the spread in the existing data is due to differing samples. Therefore, in order to understand the oxidation of Si to form SiO_2 films, it is important that the measurement of diffusion be done for thin SiO_2 films.

The present study presents the lag-time method using ellipsometry. Second, the method is used to obtain

data and then an interpretation is presented. The application of this lag-time technique has enabled the measurement of D associated with oxygen transport in SiO_2 at 1000°C and has shown that a lag-time is not observed at 900°C and below. In addition, it was discovered that linear parabolic kinetics obtain at the outset of oxidation for temperatures of 900°C and below, even for films 1000 nm thick. These experimental results lead to considering alternatives to pure Fickian diffusion as the dominant mode of transport of oxygen through SiO_2 films at the lower oxidation temperatures.

Experimental Procedures

Sample preparation.—The experimental technique utilizes SiO_2 films grown by the oxidation of single crystal silicon. The starting silicon wafers were commercially available chem-mechanically polished 2 $\Omega\text{-cm}$ p-type with (100) orientation. The silicon was cleaned by a previously outlined procedure (7) and the starting SiO_2 films were prepared via thermal oxidation in dry O_2 at 1000°C .

Ellipsometry.—The automated ellipsometer used for the present study, as well as optical constants and procedures, was previously described (7, 17). The ellipsometer can measure oxide growth while the sample is under oxidation conditions. A typical experiment is started by placing a previously grown SiO_2 film of about 10^4 \AA on an Si wafer in the oxidation furnace of the automated ellipsometer. The sample is then heated at 1000°C in either N_2 or Ar for about 20 hr. The film thickness is periodically measured to check the quality of the N_2 or Ar and to provide baseline initial oxide thickness data. At some arbitrary time after outgassing, the temperature is adjusted and equilibrated at the desired value and the ambient is switched to oxygen. Before and after this ambient change, SiO_2 thickness is measured continuously. The experiment is usually continued for more than 40 hr after O_2 is turned on to insure that steady-state oxidation is achieved.

In order to insure that any change noticed by ellipsometry is due to a change in SiO_2 thickness and not perhaps a change in optical absorption, a separate experiment was performed. A disk of optical quality fused silica of about 0.64 cm thick and 2 cm in diameter polished on one face and purposely frosted on the other face was placed in the ellipsometer furnace. The polished surface was monitored by ellipsometry and Δ and Ψ data were taken at various temperatures between 600° and 1000°C before and after switching the ambients. No change in the optical constants of the fused silica was observed. Therefore, any change observed

* Electrochemical Society Active Member.

Key words: steady-state oxidation, ellipsometry, oxidant transport.

for the thick SiO_2 films on Si would be attributed to a real change in the SiO_2 film thickness. As is shown below, this lag-time experiment performed at or below 900°C yielded initial oxidation rates equal to final rates, i.e., no lag-time. Without the experiment above, this observation could possibly be trivially explained by a difference in the optical constants of the oxide in N_2 or O_2 when the ambient is switched. On the other hand, the rapid attainment of steady-state oxidation at the lower experimental temperatures has mechanistic implications and this is covered in the Discussion section.

The temperature range 1000°–600°C was explored; higher temperatures could not be attained in the present equipment.

Lag-Time Method

The lag-time method (10,11) is based on the existence of a time delay for the transport of a gas through a membrane that initially has zero concentration of the gas. The time delay is measured from the time the temperature-equilibrated membrane contacts the gas ($t = 0$) to the time the gas appears in the other side of the membrane as a steady-state flow.

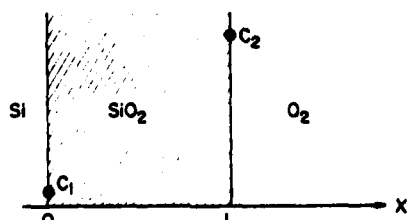
The lag-time analysis due to Daynes (10) and Barrer (11) is herein adapted to the Si- SiO_2 -oxygen system. The key equations and boundary conditions are reproduced below with some modification from the published detailed analysis (10,11). For the Si- SiO_2 -oxygen gas system, the boundary conditions are shown in Fig. 1 and the general solution for concentration is

$$C = C_1 + (C_2 - C_1) \frac{X}{L} + \frac{2}{\pi} \sum_{m=1}^{\infty} \left(\frac{C_2 \cos n\pi - C_1}{n} \right) \left(\sin \frac{n\pi X}{L} \right) \exp \left(\frac{-Dn^2\pi^2 t}{L^2} \right) + \frac{4C_0}{\pi} \sum_{m=0}^{\infty} \frac{1}{(2m+1)} \sin \frac{(2m+1)\pi X}{L} \exp \left(\frac{-D(2m+1)^2\pi^2 t}{L^2} \right) \quad [1]$$

where C is the concentration of oxidant at any time. At the Si- SiO_2 interface, $X = 0$ and

$$\left(\frac{\partial C}{\partial X} \right)_{X=0} = \frac{C_2 - C_1}{L} + \frac{2}{L} \sum_{n=1}^{\infty} (C_2 \cos n\pi - C_1) \exp \left(\frac{-Dn^2\pi^2 t}{L^2} \right) + \frac{4C_0}{L} \sum_{m=0}^{\infty} \exp \left(\frac{-D(2m+1)^2\pi^2 t}{L^2} \right) \quad [2]$$

The rate at which gas, C_g , emerges from a membrane of unit area at $X = 0$ is given as



$C = C_1$ AT $X = 0$ FOR ALL t

$C = C_2$ AT $X = L$

$C = C_0$ FOR $0 < X < L$ AT $t = 0$

Fig. 1. Pictorial representation of Si- SiO_2 - O_2 system with boundary conditions.

$$\frac{\partial C_g}{\partial t} = D \left(\frac{\partial C}{\partial X} \right)_{X=0} \quad [3]$$

Now substituting $(\partial C / \partial X)_{X=0}$ from above and solving for the concentration, C_g , by integration the resultant equation is

$$C_g = \frac{D(C_2 - C_1)t}{L} + \frac{2L}{\pi^2} \sum_{n=1}^{\infty} \left(\frac{C_2 \cos n\pi - C_1}{n^2} \right) \left(1 - \exp \left(\frac{-Dn^2\pi^2 t}{L^2} \right) \right) + \frac{4C_0 L}{\pi^2} \sum_{m=0}^{\infty} \frac{1}{(2m+1)^2} \left(1 - \exp \left(\frac{-D(2m+1)^2\pi^2 t}{L^2} \right) \right) \quad [4]$$

This concentration will increase toward a steady state as $t \rightarrow \infty$ and C_g approaches the line

$$C_g = \frac{D}{L} \left[(C_2 - C_1)t + \frac{2L^2}{D\pi^2} \sum_{n=1}^{\infty} \left(\frac{C_2 \cos n\pi - C_1}{n^2} \right) + 4 \frac{C_0 L^2}{\pi^2 D} \sum_{m=0}^{\infty} \frac{1}{(2m+1)^2} \right] \quad [5]$$

$$= \frac{D}{L} \left[(C_2 - C_1)t - \frac{C_2 L^2}{6D} - \frac{C_1 L^2}{3D} + \frac{C_0 L^2}{2D} \right] \quad [6]$$

The intercept of this line with the time axis yields the lag-time, τ

$$\tau = \frac{1}{(C_2 - C_1)} \left[\frac{C_2 L^2}{6D} + \frac{C_1 L^2}{3D} - \frac{C_0 L^2}{2D} \right] \quad [7]$$

If the actual experiment commences with no oxidant in the film, $C_0 = 0$, and if the reaction at Si- SiO_2 interface is fast relative to transport then $C_1 \sim 0$, then the lag-time expression reduces to the equation

$$\tau = \frac{L^2}{6D} \quad [8]$$

The condition of $C_0 = 0$ is achieved by a thorough out-gassing of the sample at 1000°C overnight and it is assumed that the network oxygen does not contribute to oxidation. The condition $C_1 \sim 0$ is consistent with the linear-parabolic model.

The steady-state condition is observed by the conformity of the thickness-time data to the linear parabolic rate law

$$t = AL + BL^2 \quad [9]$$

where t is the oxidation time for a film thickness L , and A and B are the reciprocals of the linear and parabolic rate constants, respectively.

This simplified linear-parabolic equation can be used to test for linear-parabolic kinetics in the present study. However, where the values of the rate constants are of interest, it is necessary to utilize the physical model related equation (2,7)

$$t - t_0 = A(L - L_0) + B(L^2 - L_0^2) \quad [10]$$

where L_0 and t_0 define the lower limit of applicability for the linear-parabolic model or an oxide of thickness L_0 , at the start of an experiment.

Equation (9) is easily linearized and linear least squares analysis of the t and L data according to L vs. t/L yield slope and intercept values that are used to extrapolate to the time axis at the initial oxide thickness value. This intersection yields the τ value used with the average L value in Eq. (8) to obtain D .

To insure that steady state is achieved, oxidation is carried out for more than 40 hr. Thickness-time data from the last 10 hr are analyzed as steady-state values. However, prior to any data analysis, the overall L , t data is sampled in the first and second hours of oxidation and then after 20, 30, and 40 hr. If the lag-time method is applicable, the oxidation rates should be initially low and then increasing toward steady state. This information provides the basis for the lag-time analysis.

Results and Discussion

In order to assess the range of possible lag-time values, τ values were calculated from the divergent D values of Norton (12) and Williams (13) and the results are shown in Table I. It is seen that if Norton's values for D are applicable for SiO_2 films, then τ is virtually unmeasurable by the present technique down to 800°C and marginally measurable down to 600°C. However, based on Williams' data, τ can be easily measured at 1000°C and below. Therefore, if the measured D values for oxidant in the SiO_2 films used for this study are near Norton's (12) values, we would expect to see no lag-time for the higher temperatures while if Williams' (13) D values obtain, a lag-time would be observed for all temperatures, and for both sets of D values the τ values would be larger for the lower temperatures. The experimental data which consist of thickness-time measurements on films with starting thickness of about 10^4 Å were first surveyed to determine whether lag-times were observed. As previously stated, this was done by comparing the rates of oxidation at the beginning of the experiment to rates at the end. At least two data sets were obtained at each experimental temperature with substantially the same results. Table II lists the rates from one data set at each temperature for the 1st, 2nd, 20th, 30th, 40th hours of the experiment. It is clearly seen that only at 1000°C is true lag-time behavior observed, i.e., the rate of oxidation increases to a steady-state value. It is also interesting to note that a steady-state rate of about 41 A/min at 1000°C for $10^4 \text{ Å} \text{ SiO}_2$ can be calculated from the derivative of Eq. [10] and already published data (18). Given that there could be a maximum of about 10% error in the reported rate constants (7), the rates for the first 2 hr are below the steady-state rate. This calculated result is in agreement with the experimental result to follow and also the steady-state rates of the present study agree with the published values. For the lower temperatures, the initial rates are at least equal to the final rates. There is some data that show a slight trend toward the initial rate being larger than the final rates. However, this type of behavior is anticipated based on linear parabolic kinetics. Representative SiO_2 thickness vs. oxidation time data is shown as Fig. 2a and 3a for 1000° and 800°C, respectively. The solid lines on these plots are drawn to illustrate the change in the slope of the data and are obtained as average slopes calculated from the data for a number of the initial and final data points (see Table II). The 1000°C data have a smaller initial slope than for long times and the opposite is true at 800°C.

Figures 2b and 3b show plots of L vs. t/L at 1000° and 800°C, respectively. The solid lines on these plots are the result of fitting the steady-state data to Eq. [9]. It is clear that the 800°C data are well represented

Table II. Comparison of initial and final rates of oxidation

T (°C)	Oxidation rates (A/hr)				
	1st	2nd	20th	30th	40th
1000	33	37	38	44	44
900	20	18	20	20	21
800	10	9	9	9	8
700	2	2	2	3	2
600	0.7	0.5	0.4	0.3	0.3

by the linear-parabolic model and this was also typical for the 900°, 700°, and 600°C data. The 1000°C data show the expected deviation for shorter times which is indicative of the existence of a lag-time. The 1000°C data were analyzed by linear least squares fitting of L vs. t/L at long times and then finding the intersection of this line with the t/L axis. The intersection is τ/L_0 where L_0 is the starting oxide thickness. τ is then used in Eq. [8] to calculate a value for the diffusion constant, $D = 2.3 \times 10^{-13} \text{ cm}^2/\text{sec}$ at 1000°C in dry O_2 . This value is about one order of magnitude larger than Williams' (13) value at 1000°C. The value for the lag-time is $\tau = 8490 \text{ sec}$. It is interesting to compare this value for τ with the value of 8804 sec calculated from the formula derived by considering the approach to steady-state flow through a plane sheet by Crank (19)

$$\frac{Dt}{L^2} \approx 0.45 \quad [11]$$

From the relationship between permeability, P , diffusivity, D , and solubility, S

$$S = \frac{PL}{D} \quad [12]$$

which applies when Henry's law is obeyed, the solubility can be calculated. The permeability is the steady-state oxidant flux which is calculated from the rate of oxidation. At 1000°C the permeability is about $P = 2.7 \times 10^{-12} \text{ O}_2 \cdot \text{cm}^{-2} \text{ sec}^{-1}$ for 1 atm O_2 pressure. This yields a value for solubility of $S = 1.2 \times 10^{21} \text{ cm}^{-3}$ which is considerably higher than Deal's (2) value of $5.2 \times 10^{16} \text{ cm}^{-3}$ calculated using the relationship

$$S = \frac{k_{\text{PAR}} \cdot 2.25 \times 10^{22}}{2D} \quad [13]$$

and Norton's (12) value for D , where k_{PAR} is the parabolic rate constant. The reason for the large difference in S values in the present study and Deal's study (2) is due primarily to differences in D . Using the value for D obtained in this study and Deal's k_{PAR} (2), S is calculated to be $1.6 \times 10^{21} \text{ cm}^{-3}$.

To determine the effect of H_2O on D , 1000 ppm was added to dry O_2 by a previously outlined procedure (20). The data at 1000°C showed a lag-time, and a value of $D = 2.4 \times 10^{-12} \text{ cm}^2/\text{sec}$ or about a tenfold increase in D with 1000 ppm H_2O was obtained. From previous studies of the effect of H_2O on the rate of Si oxidation (20), we reported less than a twofold increase in rate with 1000 ppm H_2O in O_2 . From Eq. [12], if D increases by a factor of 10 and P by a factor of 2 then the solubility of oxidant in the presence of 1000 ppm H_2O must actually decrease by a factor of five.

Table I. Literature values of D and calculated values for the lag-time, τ

	T (°C)				
	1000	900	800	700	600
$D (\text{cm}^2/\text{sec})$, from Norton (12)	6×10^{-6}	3×10^{-6}	9×10^{-10}	3×10^{-10}	5×10^{-11}
$\tau (\text{sec})$ for $10^4 \text{ Å} \text{ SiO}_2$	0.3	0.6	2	7	32
$D (\text{cm}^2/\text{sec})$, from Williams (13)	2×10^{-14}	9×10^{-12}	3×10^{-14}	7×10^{-16}	1×10^{-16}
$\tau (\text{sec})$ for $10^4 \text{ Å} \text{ SiO}_2$	8×10^4	2×10^5	8×10^6	2×10^9	2×10^7

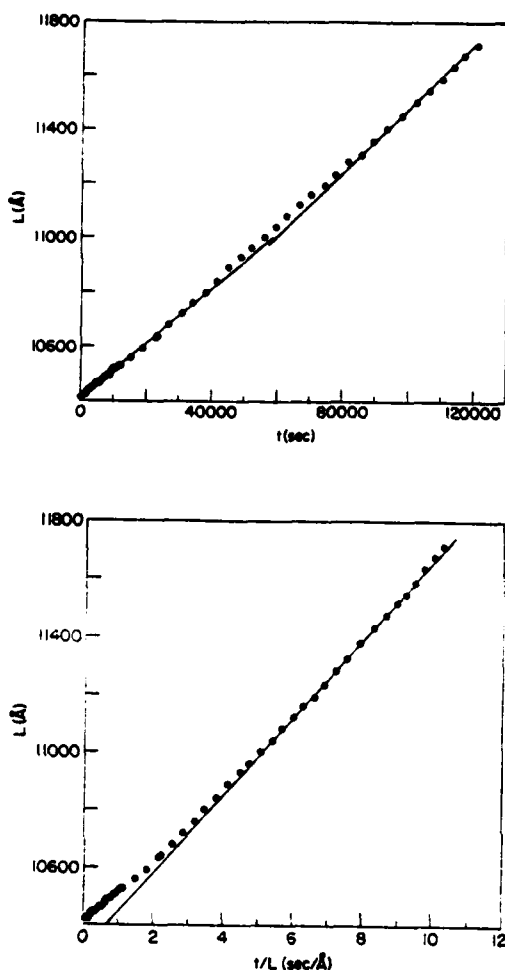


Fig. 2. Thickness, L , and time, t , oxidation data for dry O_2 at $1000^\circ C$: (a, top) as L vs. t , (b, bottom) L vs. t/L .

This result may indicate that, although trace amounts of H_2O enhance diffusion of oxidant so that the rate of oxidation increases, the H_2O ties up many active sites in SiO_2 thereby lowering the solubility of O_2 .

In terms of the mechanism of oxidation, the present results demonstrate the existence of a change in the dominant mechanism for oxidant transport near $1000^\circ C$. Above this temperature, the transport can be considered Fickian with undissociated oxygen as the likely transported species. This latter contention is based on the observation that Henry's law is obeyed at high temperatures (2). The question of whether any transported species are charged is not addressed in this study. Further evidence for the change in predominant mechanism of oxidation was obtained from an earlier study (18) in which considerable curvature in Arrhenius plots involving both linear and parabolic rate constants was reported. In that study (18), the higher temperatures yielded a lower activation energy for k_o , in agreement with earlier studies (2) that also emphasized oxidation temperatures above $1000^\circ C$. The lower temperatures yielded activation energies for k_o more than 50% larger (18). The mechanism for oxidation below $1000^\circ C$ is likely to involve a superposition of Fickian diffusion which is predominant at higher temperatures with at least one additional mode of transport. Excluding models which involve charged species, two kinds of mechanisms come to mind which would explain the rapid attainment of steady-state oxidation. One model considers the migration of atomic oxygen from network position to network position.

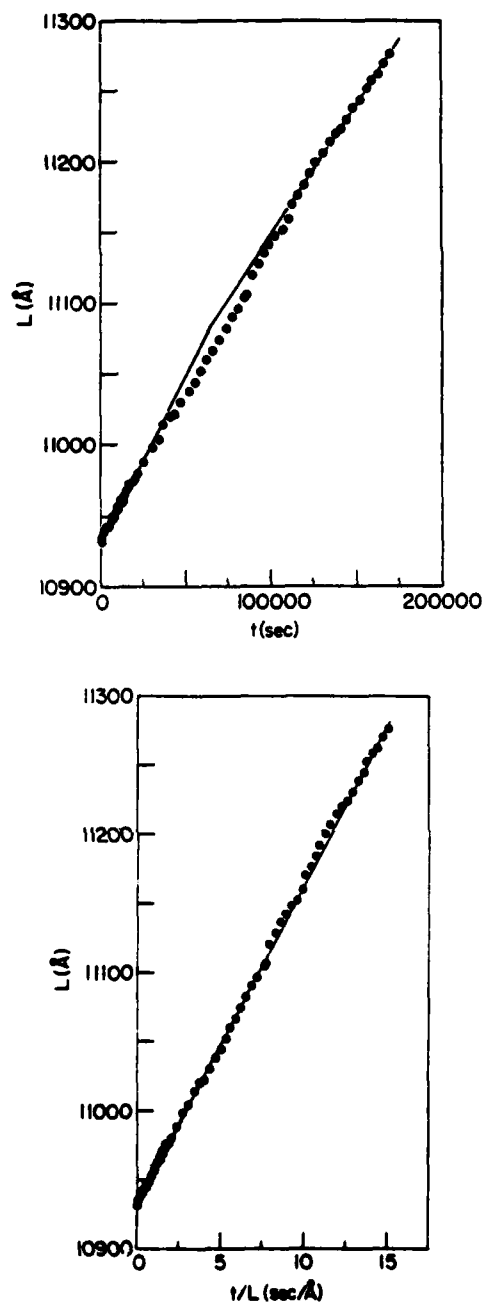


Fig. 3. Thickness, L , and time, t , oxidation data for dry O_2 at $800^\circ C$: (a, top) as L vs. t , (b, bottom) L vs. t/L .

Such a mechanism does not require long distance migration of oxygen to initiate oxidation. Rather, when one atom of oxygen is taken into the network at the gas- SiO_2 interface, an atom then becomes available at the $Si-SiO_2$ interface for oxidation. This process takes place on a time scale of atomic vibrations and would therefore explain the rapid attainment of steady-state behavior. However, the recent tracer studies of Rosencher et al. (21) and Pfeffer and Ohring (22) demonstrate that oxygen is transported across the oxide with little or no interaction with the network. Another possibility is to consider the flow of oxidant in micropores. If micropores exist in sufficient numbers and if the pores penetrate to the $Si-SiO_2$ interface then very slow diffusion at low temperatures may be short circuited by the flow of oxidant in micropores. Previous studies on thin SiO_2 films yielded some indirect evi-

dence for the existence of micropores in SiO_2 films (23) and recent transmission electron microscopy studies by Gibson and Dong (24) have shown micropores of about 10 Å to exist in dry O_2 grown SiO_2 films. Further work on a micropore model is necessary and in progress, but it is interesting to note that if Knudsen-Poiseuille flow is considered in micropores (25) in steady state with linear surface kinetics a linear-parabolic type rate law can be derived. The fact that lower oxidation temperatures yield higher density SiO_2 (26, 27) probably also contributes to a decrease in the importance of simple diffusion and perhaps renders a different transport mechanism dominant at lower oxidation temperatures.

Meek (28) has attempted to explain the large discrepancy between Norton (12) and Williams (13) measurements of D for oxygen in fused silica based on the differences in the experimental techniques, viz., Norton measures chemical diffusion based on a lag-time while Williams measures the transport of a radioisotope. According to Meek's interpretation, Williams measured value of D is necessarily smaller than Norton's due to the fraction of time the radioisotope spends in exchanging with the network rather than in the interstices of SiO_2 . Recently, however, two definitive studies (22, 29) have appeared in the literature which show that the transported oxygen does not exchange to any measurable extent with the SiO_2 network. Therefore, it is now clear that Meek's argument does not apply and the large differences in the D data can be explained either trivially by experimental errors or by real differences in the SiO_2 itself. It is quite clear that both Pfeffer and Ohring (22) and Rigot et al. (29) find large differences in the behavior of oxygen in SiO_2 when H_2O is present and it is not unreasonable to speculate that impurities and perhaps even fictive temperature and other preparation conditions lead to the large reported differences in D values.

In summary, a method to measure diffusion of oxidant in growing SiO_2 films has been developed. This method is based on Fickian diffusion through a membrane and therefore can be used to test for diffusion conditions.

Diffusion of O_2 in SiO_2 as the mode of oxidant transport has been found as the dominant mechanism at 1000°C and a value of $D = 2.3 \times 10^{-12} \text{ cm}^2/\text{sec}$ has been measured. This value increases by an order of magnitude with 1000 ppm H_2O in the O_2 . At lower temperatures, a different mode of oxidant transport is dominant. This mode is characterized by the instantaneous achievement of steady state linear-parabolic oxidation kinetics.

Acknowledgments

The author gratefully acknowledges R. Ghez for helpful discussions on the theory of diffusion and for critically reading this manuscript, to D. Dong for advice with experimental procedures, and to D. R. Young for suggesting the possible use of ellipsometry for the measurement of D .

Manuscript submitted Jan. 13, 1981; revised manuscript received Aug. 4, 1981. This was Paper 518 presented at the Hollywood, Florida, Meeting of the Society, Oct. 5-10, 1980.

Any discussion of this paper will appear in a Discussion Section to be published in the December 1982 JOURNAL. All discussions for the December 1982 Discussion Section should be submitted by Aug. 1, 1982.

Publication costs of this article were assisted by IBM Corporation.

REFERENCES

- U. R. Evans, "The Corrosion and Oxidation of Metals," Chap. XX, Edward Arnold Ltd., London (1960).
- B. E. Deal and A. S. Grove, *J. Appl. Phys.*, **36**, 3770 (1965).
- W. A. Pliskin, *IBM J. Res. Dev.*, **10**, 198 (1966).
- M. M. Atalla, in "Properties of Elemental and Compound Semiconductors," H. Gatos, Editor, p. 163, Interscience Inc., New York (1960).
- J. R. Ligenza and W. G. Spitzer, *J. Phys. Chem. Solids*, **14**, 131 (1960).
- W. A. Pliskin and R. P. Gnall, *This Journal*, **111**, 872 (1964).
- E. A. Irene and Y. J. van der Meulen, *ibid.*, **123**, 1380 (1976).
- A. G. Revesz and R. J. Evans, *J. Phys. Chem. Solids*, **30**, 551 (1969).
- M. A. Hopper, R. A. Clarke, and L. Young, *This Journal*, **122**, 1216 (1975).
- H. A. Daynes, *Proc. R. Soc. London, Ser. A*, **97**, 286 (1920).
- R. M. Barrer, "Diffusion In and Through Solids," Chap. I, Cambridge University Press, London (1951).
- F. J. Norton, *Nature (London)*, **171**, 701 (1961).
- E. L. Williams, *J. Am. Ceram. Soc.*, **48**, 190 (1965).
- R. Haul and G. Dümen, *Z. Electrochem.*, **66**, 636 (1962).
- E. W. Sucov, *J. Am. Ceram. Soc.*, **46**, 14 (1963).
- R. Roy, *J. Non-Cryst. Solids*, **3**, 33 (1970).
- Y. J. van der Meulen and N. C. Hien, *J. Opt. Soc. Am.*, **64**, 804 (1974).
- E. A. Irene and D. Dong, *This Journal*, **125**, 1146 (1978).
- J. Crank, "Mathematics of Diffusion," p. 49, Oxford University Press, London (1956).
- E. A. Irene and R. Ghez, *This Journal*, **124**, 1757 (1977).
- E. Rosencher, A. Straboni, S. Rigo, and G. Amsel, *Appl. Phys. Lett.*, **34**, 254 (1979).
- R. Pfeffer and M. Ohring, *J. Appl. Phys.*, To be published.
- E. A. Irene, *This Journal*, **125**, 1708 (1978).
- J. M. Gibson and D. Dong, *ibid.*, **127**, 2722 (1980).
- R. M. Barrer, "Diffusion In and Through Solids," Chap. II, Cambridge University Press, London (1951).
- E. A. Taft, *This Journal*, **125**, 968 (1978).
- E. A. Irene, D. Dong, and R. J. Zeto, *ibid.*, **127**, 396 (1980).
- R. L. Meek, *J. Am. Ceram. Soc.*, **56**, 341 (1973).
- S. Rigo, F. Rochet, A. Straboni, and B. Agius, in "International Conference on Physics of MOS Insulators," North Carolina State University, Raleigh, NC, June 1980.

**This work was sponsored by Defense Advanced Research Projects Agency (DoD) ARPA Order No. 4012 Under Contract No. MDA903-81-C-0100 issued by Department of Army, Defense Supply Service-Washington, Washington D.C. 20310